DESIGN OF A 2 D.O.F. HAPTIC DEVICE

CHRISTOPHE TAQUET

A THESIS SUBMITTED

FOR THE DEGREE OF MASTER OF ENGINEERING

DEPARTMENT OF MECHANICAL ENGINEERING

NATIONAL UNIVERSITY OF SINGAPORE

2008

Acknowledgements

I would like to thank the National University of Singapore and Supelec for giving me the opportunity to study in Singapore for my master degree. I also want to thank Dr Chew Chee-Meng for his financial support in the manufacturing of the interface, and for his supervising, as well as Prof Hong Geok-Soon and Zheng Yu for their advice. Lastly I want to thank the few people who sacrificed a bit of their time for the experiments.

Table of Contents

Acknowledgements ……... i

Table of Contents ……. ii

Summary ……... v

List of Tables ……..... vi

List of Figures ……... vii

List of Abbreviations ..……. ix

1. INTRODUCTION ……... 1

1.1 Virtual reality and haptics ……... 1

1.2 Overview of haptic interfaces …….. 1

1.3 Hybrid interface ……... 4

1.4 Goals of the project …….. 6

2. DEVICE DESIGN AND SETUP ……..... 8

2.1 Detailed physical design and considerations……..…….. 8

2.2 Choice of components ……. 10

2.2.1 Ultrasonic motor ……... 10

2.2.2 Magnetic particle-clutch …….. 13

2.2.3 Encoders ……... 15

2.2.4 Force gauge ……... 15

2.2.5 Computer equipment …… 16

2.2.6 Electrical equipment ……. 16

2.3 Mathematical model…… 17

2.4 Workspace……... 18

3. COMPONENTS TESTING……..... 21

3.1 Ultrasonic motor..…… 21

3.1.1 Input-output characteristic……... 21

3.1.2 Dynamic performance……... 22

3.2 Magnetic particle-clutch…….. 25

3.2.1 Input-output characteristic……... 25

3.2.2 Dynamic performance……... 26

3.3 Haptic device……...…….. 28

4. HAPTIC INTERFACE EVALUATION……..... 30

4.1 Evaluation according to the three necessary criteria…… 30

4.1.1 Free space must feel free……..……. 30

4.1.2 Solid virtual object must feel stiff..……... 31

4.1.3 Virtual constraints must not be easily saturated.……... 32

4.1.4 Comparison with other interfaces…….. 33

4.2 Force bandwidth……... 35

4.3 Force-field simulation……... 37

4.3.1 Free Space.……... 37

4.3.2 Wall.……..…… 39

4.3.3 Coulomb Friction.…….. 40

5. CONCLUSION AND FUTURE RESEARCH…….. 42

Bibliography ……. 43

Appendix: Arm model …… 49

Summary

This thesis describes the design and the testing of a two-degree-of-freedom haptic interface. The purpose of the interface is to evaluate the performance that can be achieved using an ultrasonic motor in series with a magnetic particle clutch as actuators for each degree of freedom. The combination of these two components will result in a hybrid actuator, which has active and passive operation modes. The device was designed to feature low undesirable dynamics and low inertia. Each component was evaluated individually to find out its influence on the performance of the interface. The interface's characteristics were compared to other common devices. Several force-fields were implemented to test the overall feeling of the user during manipulation. It turned out that the ultrasonic motor had better force capabilities in continuous mode, and that the magnetic particle clutch improved the stability of the interface, especially when simulating passive force fields.

List of Tables

Table 2.1: USR60 specifications..... 12

Table 2.2: Motor comparison.....; 13

Table 2.3: Magnetic particle-clutch specifications..... 15

Table 4.1: Interfaces comparison..... 34

List of Figures

Figure 1.1: Teleoperation principle ……... 2

Figure 2.1: Design of the arm ……..... 9

Figure 2.2: MPC's S-shape current vs torque characteristic …….. 14

Figure 2.3: Sketch of the arm ……. 18

Figure 2.4: Tip workspace …….…….... 20

Figure 3.1: Rotational speed of the USM versus input voltage …….……... 21

Figure 3.2: Speed response of the USM to a step command ……. 22

Figure 3.3: Bode diagram for USM speed response …….…….……... 23

Figure 3.4: Speed response with zero-crossing (up), and without (down)……. 24

Figure 3.5: Torque measurement setup 25

Figure 3.6: Current – torque characteristic of the MPC ….…….. 26

Figure 3.7: MPC response to torque step input ……. 27

Figure 3.8: Achievable velocity direction (dark) and non-achievable (light)…….... 29

Figure 4.1: Maximum achievable stiffness …….……... 32

Figure 4.2: Response of the tip to a force step input ……..... 36

Figure 4.3: Magnitude Bode diagram ……...…….……... 37

Figure 4.4: Trajectory of the tip when the user tries to follow a straight path …..... 39

Figure 4.5: Velocity of the tip before and after encounter with the wall ……... 40

List of Figures

Figure 4.6: Wall simulation with stiffness k = 2000 N/m ……. 40

Figure 4.7: Simulation of dry friction ……... 41

Figure A.1: Coordinates and moments definition …….. 49

Figure A.2: Force at the tip vs distance from center of rotation…...…….. 56

List of Abbreviations

A, B: inertia parameters of the arm

CW: Clockwise

CCW: Counter-clockwise

DC: Direct Current

det(J): determinant of matrix J

DOF: Degree Of Freedom

F: force at the tip

I: inertia of a link in the z direction

I/O: Input/Output

J: jacobian matrix

k: stiffness

L: length of a link

m: mass of a link

MPC: Magnetic Particle Clutch

Q_1, Q_2: generalized torques

STG: Servo To Go

USM: Ultrasonic Motor

θ: *a*ngular coordinates

τ: torques

μ_{Al}: density of aluminium

1. INTRODUCTION

1.1 Virtual reality and haptics

Virtual reality is a technology that consists of creating virtual environments simulating real events. It allows a user to interact with a computer simulated environment through his visual, auditory and tactile senses. Most virtual environment systems are visual, the head mounted display being one of the most famous ones.

Haptics is the branch of virtual reality that refers to the sense of touch. It lets the user interact with the virtual environment by means of force through a haptic interface. Compared with visual interfaces, haptics proves to be more challenging. Indeed, visual interfaces display an environment to the user, and the user's vision cannot influence the interface. Haptic interfaces give force to the user, but the user influences the interface as well by the force he applies. There is an active interaction between the user and the interface. This bidirectional flow of information makes haptics a real challenge.

1.2 Overview of haptic interfaces

There are many different haptic interfaces available today. They can serve many different purposes from simple entertainment to sophisticated applications in industrial, scientific or medical fields.

The use of haptics is widely spreading nowadays. However most of its applications are still being perfected, but the expectations are very high. The most impressive applications of haptic devices are probably in the field of telerobotics. The mechanism is explained in Figure 1.1. Telerobotics involves two robots linked to each other by commands and

sensor information. The user will manipulate a master robot, giving motion and force to it. The information will then be sent to a slave robot that will react accordingly. For example, telesurgery relies on this principle. The surgeon is physically separated from the workplace. From another place, he will manipulate a master robot instead of his usual tools, which are replaced by robotic ones. However he keeps full control of the operation through teleoperation as the motion he gives to the master robot will be sent as commands to the slave robot. This technique brings great advantages. For example, Hunter et al [1] developed a micro-surgical device that scaled down the movements performed by the surgeon with the master manipulator. These scaled movements are then reproduced by the slave micro-movement robot, giving the surgeon better virtual sensitivity. Still based on the master-slave robot interaction, haptics can be of great help in robotics, especially in human hostile environments. Kazerooni et al.[2] designed a separate carrier, where the user moved a light master robot ant its motion was reproduced by the slave robot. Force feedback would enable the user to perform more delicate tasks.

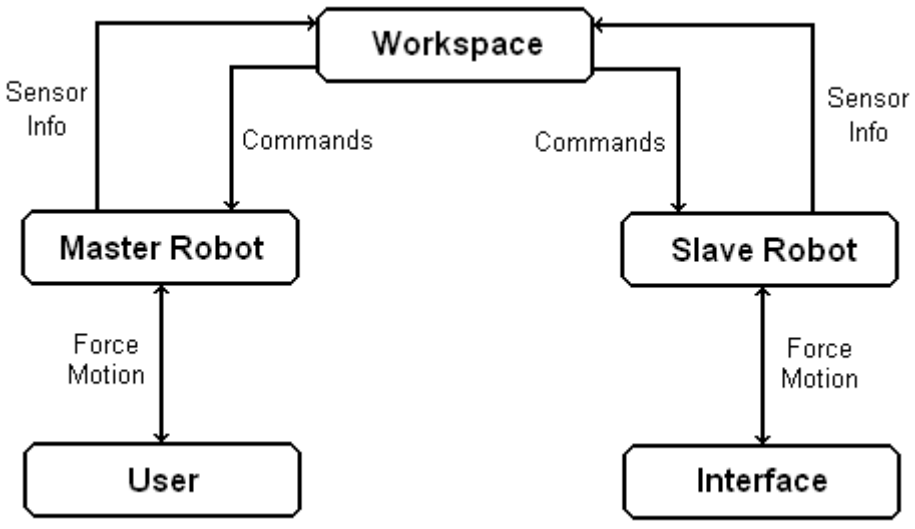

Figure 1.1: Teleoperation principle

While these applications are still not commonly used with force feedback, haptic devices with force feedback have helped researchers in understanding better how human being reacts to the sense of touch [3, 4]. It is also widely used in situations with limited availability or when danger is involved: training soldiers in war situations, training future pilots in flight simulators, or training surgeons [5].

Haptics are also being used for rehabilitation purposes. Bergamasco and co-workers [6] have worked on hand and arm exoskeletons, consisting of a skeleton-like framework worn by a person, to help people recover their natural motion. Switzerland researchers created the Lokomat® for assisting people in their locomotion rehabilitation [7]; the Lokomat is now in use in many reeducation centers.

However the most famous application of haptics is probably in the entertainment field. The consumer market offers a wide range of entertaining haptic device enabled with force feedback such as joysticks, steering-wheels and mouses. They are mainly used with video games. Compared to usual devices, they bring new sensations to the user by applying a force to him, making games more realistic. For example, the Microsoft SideWinder series offers some joysticks with force feedback. Other than computer related devices, some mobile phones are equipped with tactile feedback touchscreens, such as the Samsung SCH-W559. When the user presses a button on the touchscreen, he feels he is pressing a mechanical button. Another interface worth mentioning is the Novint Falcon™ developped by Novint Technologies and specifically designed for the gaming world, providing real-time 3D force interaction at an affordable price [8].

There exists many commercialized haptic devices intended for general purposes. The Phantom® interfaces by Sensable are among the most famous general purpose interfaces.

The Phantom® series has a serial mechanical structure and includes products ranging from small interfaces like the Phantom® Omni™, a 3 DOF desktop interface, to stronger 6 DOF interfaces like the Phantom Premium™ [9]. As opposed to the Phantom® series, Force Dimension has designed parallel structure interfaces like the Omega™ series and the Delta™ series, a more powerful version than the Omega™ series [10]. Haption also has its own series, the Virtuose™, which includes the Virtuose™ 6D40-40 dedicated to teleoperation and the INCA 6D, a large-scaled wire based interface [11]. Quanser developped 3 DOF and 5 DOF interfaces for research purposes [12], while MPB designed the Freedom™ 6S and 7S for medical simulation and master/slave robotics [13].

1.3 Hybrid interface

Haptic interfaces can be classified as active or passive. Active interfaces would interact with the user by providing energy thanks to active actuators, typically motors. On the contrary, passive interfaces would absorb energy from the system, using energy dissipating components such as brakes or dampers.

Most interfaces have focused on using active actuators, as they can provide active forces. However one of their drawbacks is that they can generate additional unwanted energy, thus provoking instability and endangering the user's safety. A lot of research was conducted so as to reduce this unwanted energy. Energy based approaches were used in [14, 15] to find out the causes of this energy excess and provide stability conditions. [16] found out that passivity was sufficient for stability but not strictly necessary. According to [15], one of the causes of hte generation of excess energy is the time delay due to the zero-order hold, that creates instability, if the haptic device's intrinsic friction didn't

dissipate it. Ellis et al. proposed numerical methods to reduce the energy excess, by predicting the position of the device at the next time step [17], while Hannaford and Ryu used passivity control schemes for dynamically estimating the energy generation and dissipating it through a digital damper element [18] and Stramigioli and co-workers tracked and dissipated energy excess by a port-Hamiltonian approach [19]. More work has been done to investigate the role of quantization [20], Coulomb friction [21] and computational delay [22], in preserving system stability.

However the implementation of such control schemes remains bulky and complicated to design. The addition of a dissipative element to the interface is a solution to ensure its passivity, though it raises other issues, for example on the mechanical design complexity. The addition of a dissipative element would provide physical damping to the system, therefore ensuring passivity of the system. Indeed, passive components present the advantage of being intrinsically stable as they can only remove energy from a system. The university of Toronto developed a spring-like passive device, that stores and releases the energy given be the user [23], while Pai, et al designed a similar interface, adding pressure sensors [24]. Other passive haptic devices were developed using purely dissipative elements. Swanson and Book designed a redundant 2 DOF passive haptic device using two brakes, and two clutches [25], while Koyanagi, et al. developed a 2 DOF redundant passive haptic device with four electro-rheological brakes [26]. These systems had better stability, and improved the safety of the user. However they could not simulate any active forces.

Hybrid interfaces are a natural extension of these passive and active interfaces. These interfaces contain active actuators and passive components. An and Dong designed a 1

DOF hybrid joystick, using a DC motor as active actuator and a magneto-rheological brake as passive actuator [27]. A 3 DOF force reflecting joystick was developed by Russo and Tadros, with three motors directly in series with magnetic brakes [28].

1.4 Goals of the project

This project consists of designing and testing of a 2 DOF hybrid haptic interface for general purposes. For each link, the actuator is the result of the combination of a passive actuator with an active actuator. The passive actuator chosen is a magnetic particle clutch (MPC), while the active actuator is an ultrasonic motor (USM). The resulting actuator will be a hybrid actuator controllable in torque and speed. When using only a purely active actuator, the energy given to the actuator by the user through the interface cannot be easily dissipated, causing instability. It is expected that the use of a passive actuator will help to absorb this energy, and thus improve the stability.

Many different criteria have been used for the evaluation of the overall performance of a haptic interface [14, 29, 30, 31, 32]. For our work, we will mostly use the following criteria used in [33] by Massie and Salisbury for the evaluation of the Phantom®:

(1) In low impedance areas, the user must ideally feel nothing is restricting his motion, which means that the interface should have low inertia and little friction under zero force command.

(2) In high impedance areas, the simulated objects must feel stiff. The stiffness capabilities of an interface are measured by the maximum stiffness achievable while the system remains stable.

(3) The interface's maximum force must be high enough to withstand the force applied by the user as we don't want the user to go through a wall.

As the device will be designed for general purposes, we don't have any specific requirements. We hope that the use of a passive actuator will provide more stability to our interface. Therefore we aim for achieving good results for criterion (2). We will also make sure we achieve good results for the other criteria.

2. DEVICE DESIGN AND SETUP

In this chapter, we will present our haptic interface. We will present the design of the interface and its various components, and a mathematical model will be derived.

2.1 Detailed physical design and considerations

The haptic interface is showed in Figure 2.1. It is a 2 DOF planar parallel arm. It is therefore composed of 4 links that formed a parallelogram. The first two links are commanded by two separated actuators. The last two links are linked to the first two links by passive rotational joints. They are also linked to each other by a passive rotational joint at the other ends. Any desired end-effector can be mounted at the tip of the arm.

The choice of a parallel structure is mainly due to the fact that such a structure enables both links to be actuated from the base. In our case, the actuator, which consists of the combination of the MPC and the USM is quite heavy, as the MPC itself weighs 2.25 kg. Mounting the actuator on the arm will raise obvious issues due to its weight. Ideally gravity should have no effect. The use of belts or cables can avoid the use of a parallel structure, but they introduce undesired dynamics such as mechanical backlash or friction. The parallel structure remains the best solution to deal with these problems. As the actuators are both on the base, there is no extra weight on the arm, thus all the energy will be provided for interacting with the user. Moreover parallel structures have higher rigidity than serial ones and faster time response. The error at the end-effector is also lower as it is averaged, instead of being additive as in serial robots.

To avoid as much as possible the gravity effects, the material chosen for the links is aluminum, as it is quite light and cost-effective. Moreover having light links would

reduce the inertia of the arm, allowing faster response. The length of each link had to be chosen so as to meet a compromise between the workspace area and the maximum force achievable. It is each 13.5 cm long.

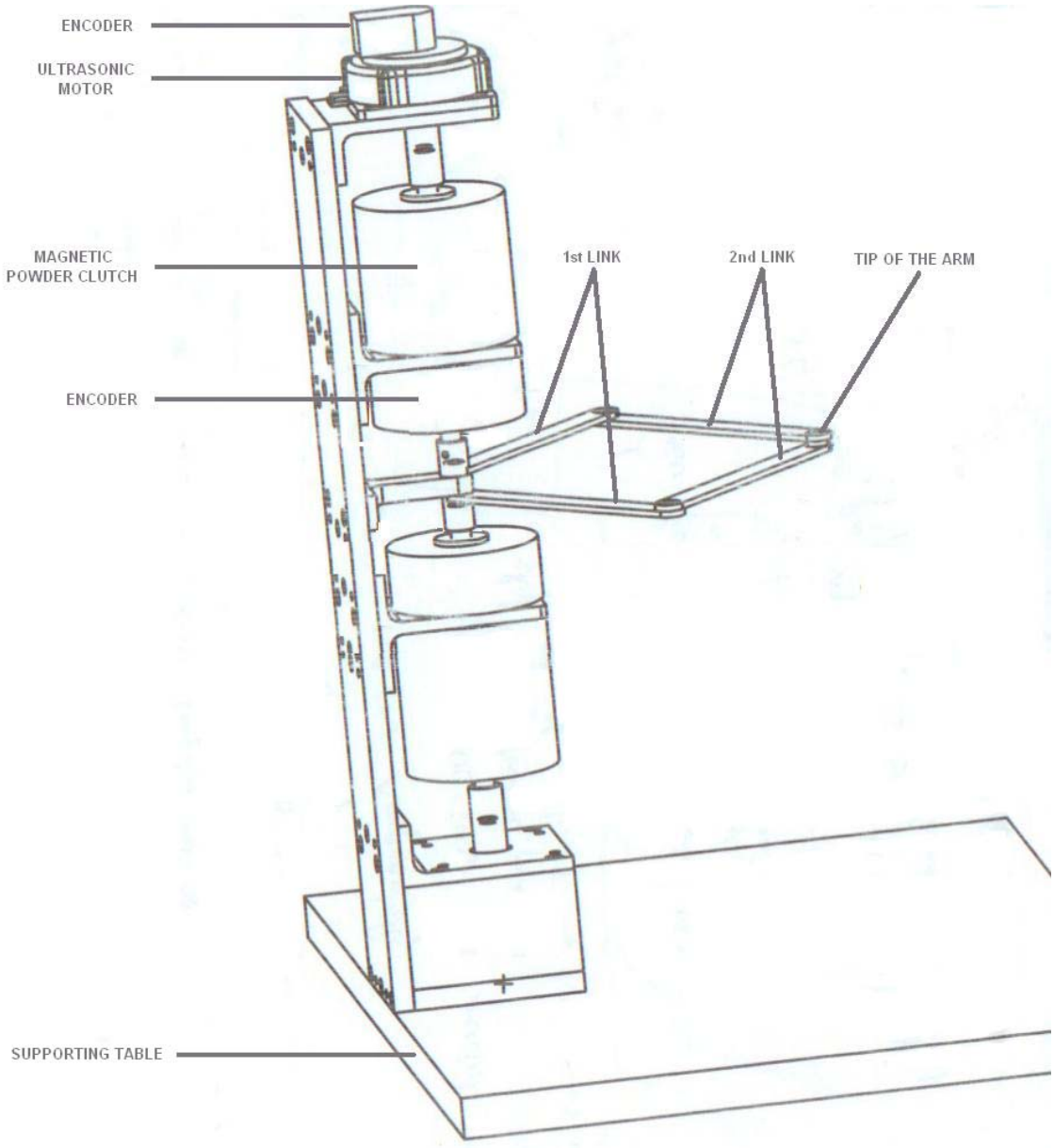

Figure 2.1: Design of the haptic device

Each actuator is constructed as follows. The output of the USM is connected to the input of the MPC. They are linked to each other by a flexure bearing. An encoder is used to measure the position of the USM shaft. The output of the MPC is connected to the robot link through a flexible coupling. A rotary hollow encoder is placed between them in order to measure the position of the first link.

Both sets of hybrid actuators are placed along the same vertical axis in order to simplify the derivation of the dynamics of the robot arm. The actuators are mounted facing each other and they are supported by a central column. Therefore the links are actuated from a fixed base. The whole system is fixed on a heavy support to ensure the whole structure would remain stationary.

2.2 Choice of components

2.2.1 Ultrasonic motor

An ultrasonic motor is a friction type motor based on the ultrasonic vibration of a stator which is placed against a rotor. The ultrasonic vibration induced in the stator is used to impart motion to the rotor.

Most haptic interfaces use electromagnetic motors as their active actuators. Compared to these motors, USM has both advantages and drawbacks, as explained in [34, 35]. The USM provides high torque at low speed, which is particularly interesting for haptic interfaces as the speeds involved are quite low. It also possesses low inertia, and thus fast dynamics. It has a high holding torque under no excitation, operates silently and is quite light and compact. But as USM are friction type motors, they have non-linear characteristics such as a load-dependent dead-zone.

We chose the USR60-E3 from Shinsei Corporation, which has a rated torque of 0.5 Nm and a maximum torque of 1 Nm. It consists of a USM and an optical incremental encoder with a resolution of 500 pulses per revolution. The datasheet is given in Table 2.1 [36]. Table 2.2 shows a comparison between some common types of electric motors and the USR60. It shows that to achieve the same rated torque, DC/AC motors tend to much heavier.

Due to the non-linear effects of USM, it is quite difficult to derive a model [34] and the design of a controller is even more difficult. However, Shinsei Corporation developed the D6060 driver dedicated to their motor. As torque controllers are still under investigation [37], this driver only allows speed control of the motor through a frequency control method. It receives a voltage command as input, and the speed of the motor would be proportional to this voltage input. The direction of rotation of the motor is commanded separately by a digital input. When CW and CCW inputs are both low, the motor will not rotate whatever the input command is. When either of them is high it will rotate accordingly and when both are high CW takes priority. A 10 ms interval is required when changing side. The motor's response time along with the driver is 50 ms.

Table 2.1: USR60 specifications

	Standard	Nonmagnetic
Driving frequency	40 KHz	
Driving voltage	130 Vrms	
Rated torque	0.5 Nm (5 Kgf-cm)	
Rated output	5.0 W	
Rated rotational speed	100 rpm	
Maximum torque	1.0 Nm and above (1.0 Kgf-cm)	
Holding torque	1.0 Nm and above (1.0 Kgf-cm)	
Responsibility	1msec or below (no inertia load or driver sweep)	
Rotational direction	CW, CCW	
Longevity	1,000 Hrs	
Service temperature range	-10℃ to +55℃	
Service temperature rise	70℃ at stator surface / 55℃at case surface	
Weight	USR60	

S3	S4	E3	S3N	S4N	E3N
260g		275g	260g		275g

Table 2.2: Motor comparison

Motor Type	Rated Speed (rpm)	Rated Torque (Ncm)	Weight (kg)
USM	100	50	0.26
Brushed DC Motor	3200	62	4
Brushless DC Motor	2860	40	1.8
AC Motor	2600	31.5	2

2.2.2 Magnetic Particle Clutch

The S90MPA-C28D37 MPC from Sterling Instrument was chosen as the passive actuator. The main reasons for using this actuator is firstly because it is passive and secondly because it is torque controllable. For haptic interfaces, torque control is primordial to render the haptic force fields. Therefore the MPC is a perfect complement to the USM which is not torque controllable. Moreover the presence of the MPC between the arm and the USM will prevent the user from being directly in contact with the actuator. The MPC will act like an energy interface between the user and the USM: it transmits the energy from the motor to the user and naturally absorbs the extra energy from the motor or the user, thus improving the stability of the system. It is also supposed to make the system perfectly stable when simulating purely passive force fields such as friction.

The MPC mainly consists of two shafts separated by a gap filled with a fine stainless steel powder, and a coil. When a current runs through the coil, it creates a magnetic field. As the output torque of the MPC is proportional to the magnetic field, it is proportional to the input current as well. When the output torque is higher than the output load, the clutch will drive without slip. On the contrary when the load torque is higher, the clutch will smoothly slip at the torque level set by the input current, independently of the slip. In fact,

the torque-current characteristic is not perfectly linear but presents an S-shape as shown in Figure 2.2 [38].

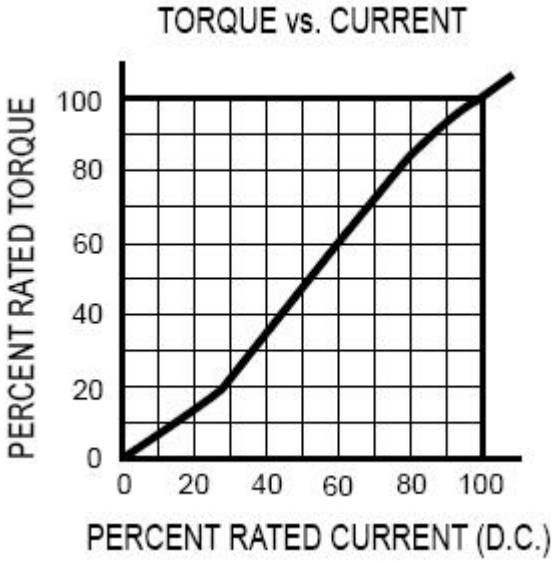

Figure 2.2: MPC's S-shape current vs torque characteristic [38]

The torque range of the clutch lays between 0.045 Nm and 1.7 Nm. Ideally, the maximum torque of the USM should have matched the maximum torque of the MPC. However, we didn't focus on choosing a model adapted to our USM. Therefore the maximum torque of the MPC is far higher than the one of the USM, but this will provide more strength to the interface when simulating purely passive force fields.

In order to drive the MPC, Sterling Instrument provides the S90MPS-24MC as power-supply for the clutch. This power-supply takes a voltage command as input, and outputs a constant current that will run through the MPC's coil. This constant current will result in a constant value for the torque.

The MPC has a 25 ms latency time before the output shaft starts moving, which is largely inferior to the 100 ms needed for a human being to perceive a movement [39] The specification of the MPC is shown on Table 2.3 [38].

Table 2.3: Magnetic particle-clutch specifications

Catalog Number	Torque Range lb. - in.	Elect. Power watts	Shaft Inertia lb. - in. - sec.^{2}	Max. Speed rpm	Mech. Heat Dissi-pation watts	Max. Overhung Load lbs.	Unforced Response msec.	Weight lbs.
S90MPA-C14D19A	0.06 - 2	3	26 x 10^{-7}	2000	6	4	9	0.7
S90MPA-C23D31	0.12 - 5	5	13 x 10^{-6}		10	20	18	3
S90MPA-C28D37	0.4 - 15	6	33 x 10^{-6}	1400	20	35	25	5
S90MPA-C34D50	0.6 - 35	10	15 x 10^{-5}	1000	30	50	70	9
S90MPA-C45D75	1 - 70	14	66 x 10^{-5}	1000	50	80	90	17
S90MPA-C52D75	4 - 130	15	15 x 10^{-4}		80		130	22

2.2.3 Encoders

There are four encoders in the system. Two of them are linked to the motors and will measure the position of the motors. The two others' function is to measure the angular position of the first links of the arm. It is fixed between the output shaft of the MPC and the first link of the arm, as it was chosen hollow as shown in Figure 2.1. The use of a hollow encoder will minimize the vertical distance between the upper links and the lower links. The RI-58-D from Hengstler was chosen.

2.2.4 Force gauge

The force measurements were done using a force gauge manufactured by Imada. The force is measured at the tip of the device. Different implements of different shapes could be fixed on this tip, so the force gauge could measure forces in different situations and adapt many end-effectors.

The force gauge comes along with a piece of software that records the force measured according to a sampling rate set by the user.

2.2.5 Computer equipment

Experiments were simulated using a 450 MHz Pentium III, running under Windows 2000 operating system. A STGII-8 model I ISA bus servo I/O card manufactured by Servo To Go, Inc was used for the communication between the computer and the system [40]. A driver is provided by STG along with the card for Windows 2000. It is compatible with both C/C++ and Visual Basic and uses a dynamic link library to communicate between the Visual Basic code and the main STG driver. As Windows is not a natural real-time operating system, a built-in timer on the STG card produces a periodic interrupt capable of interrupting the CPU. Throughout the experiments, the overall refreshing rate was 1 KHz. The STG card communicates with the outer world through 50-pin connectors connected to one of the 4 different ports of the card.

2.2.6 Electrical equipment

A 5V DC power supply is available on the STG card. It was used to supply power to the motor encoders, as they do not require high currents to work. A common power supply was used for the arm encoders and the USM drivers. This unit had two independent channels with two current limiters. It provided the 10V DC needed by the other encoders and the 24V DC needed by the drivers.

The analog output functionality of the STG card was used to control the drivers of the USM and of the MPC. The available voltage lies in a +10V/-10V span. It can be directly connected to the MPC drivers to control the torque. As the USM drivers require from 0 to 3.2 V, the analog output can be connected to them through a simple voltage divider.

Lastly, the command to choose the direction of rotation of the USMs was given by the digital output of the STG card.

2.3 Mathematical model

Using the Lagrangian approach, an ideal model of the dynamics of the system was derived, under the assumptions that no gravity forces are exerted on the arm, and no friction are induced by the rotational joints. More details are available in the appendix. A sketch of the arm is showed in Figure 2.3. This sketch will serve as reference for the equations throughout the thesis. The axes are fixed to the base.

$$\begin{pmatrix}\tau_1\\ \tau_2\end{pmatrix}=\begin{pmatrix}\mathrm{A} & \mathrm{B}\cdot\cos(\theta_2-\theta_1)\\ \mathrm{B}\cdot\cos(\theta_2-\theta_1) & \mathrm{A}\end{pmatrix}\cdot\begin{pmatrix}\ddot{\theta}_1\\ \ddot{\theta}_2\end{pmatrix} + \begin{pmatrix}0 & -\mathrm{B}\cdot\sin(\theta_2-\theta_1)\cdot\dot{\theta}_2\\ -\mathrm{B}\cdot\sin(\theta_2-\theta_1)\cdot\dot{\theta}_1 & 0\end{pmatrix}\cdot\begin{pmatrix}\dot{\theta}_1\\ \dot{\theta}_2\end{pmatrix} \quad (1)$$

where $\tau=\begin{pmatrix}\tau_1\\ \tau_2\end{pmatrix}$ denotes the joint torques , $\theta=\begin{pmatrix}\theta_1\\ \theta_2\end{pmatrix}$ denotes the joint angles, and A and B are inertia parameters determined by the arm's weight and length.

The arm's Jacobian matrix J transforms the angular velocities θ into the linear velocities of the tip V . It can also transform tip forces into joint torques, by the following equation: $\tau = J^T \cdot F$, where F is the force vector at the tip. The jacobian also allows us to detect singular configurations of the arm. The Jacobian is given by

$$J=\mathrm{L}\cdot\begin{pmatrix}-\sin(\theta_1) & -\sin(\theta_2)\\ \cos(\theta_1) & \cos(\theta_2)\end{pmatrix} \quad (2)$$

where L is the length of one link of the arm.

Singular configurations occur when $\det(J)=0$, which yields

$$\sin(\theta_1)\cdot\cos(\theta_2)-\cos(\theta_1)\cdot\sin(\theta_2)=0$$

Finally, we can deduce that singularities occur when $\theta_1=\theta_2+k\cdot\pi,\quad k\in Z$.

The latter condition corresponds to the following two geometrical configurations:

- $\theta_1-\theta_2=0$: the arm is fully exerted
- $\theta_1-\theta_2=\pi$: the arm is fully contracted

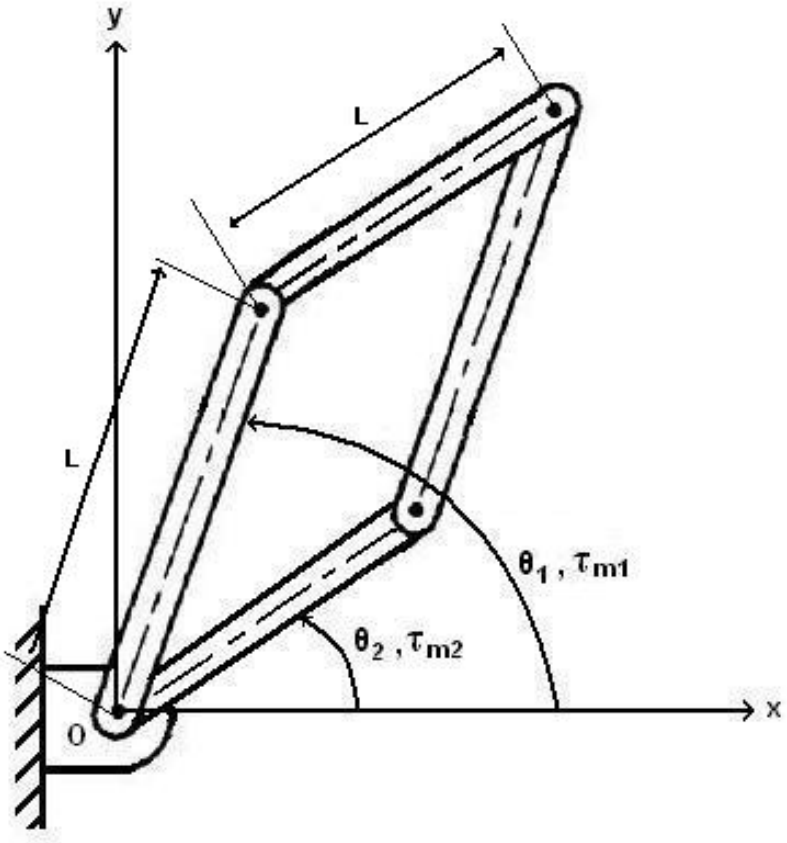

Figure 2.3: Sketch of the arm

2.4 Workspace

The theoretical reachable workspace for such an arm would be a disk of radius $2\cdot L\approx 27\,cm$. However the practical workspace is reduced due to mechanical constraints and for safety reasons.

First, the arm is mechanically constrained to $\theta_1 > \theta_2 + 0.1\,\text{rad}$ by a mechanical stop. This will avoid redundancy, and will prevent the arm of approaching too near to the singular configuration $\theta_1 = \theta_2$. Avoiding singular configurations will reduce the chances of overflow in the program.

Then, the presence of wires conducting high currents raises safety issues. These wires are placed near the central column. As a consequence, we don't want the links to approach to near from the central column, hence the following travel limitation was implemented: $(\theta_1, \theta_2) \in \left[-\frac{\pi}{2} + 0.1 \ , \ \frac{\pi}{2} \right] \times \left[-\frac{\pi}{2} \ , \ \frac{\pi}{2} - 0.1 \right]$.

Lastly, in order to avoid the tip to bump into the central column supporting the actuators, another travel limitation was implemented to constrain the arm to $\theta_1 - \theta_2 < \pi - 0.2\,\text{rad}$. It will avoid as well the arm to approach the singular configuration $\theta_1 - \theta_2 = \pi$. The reachable workspace of the tip of the arm is plotted in Figure 2.4.

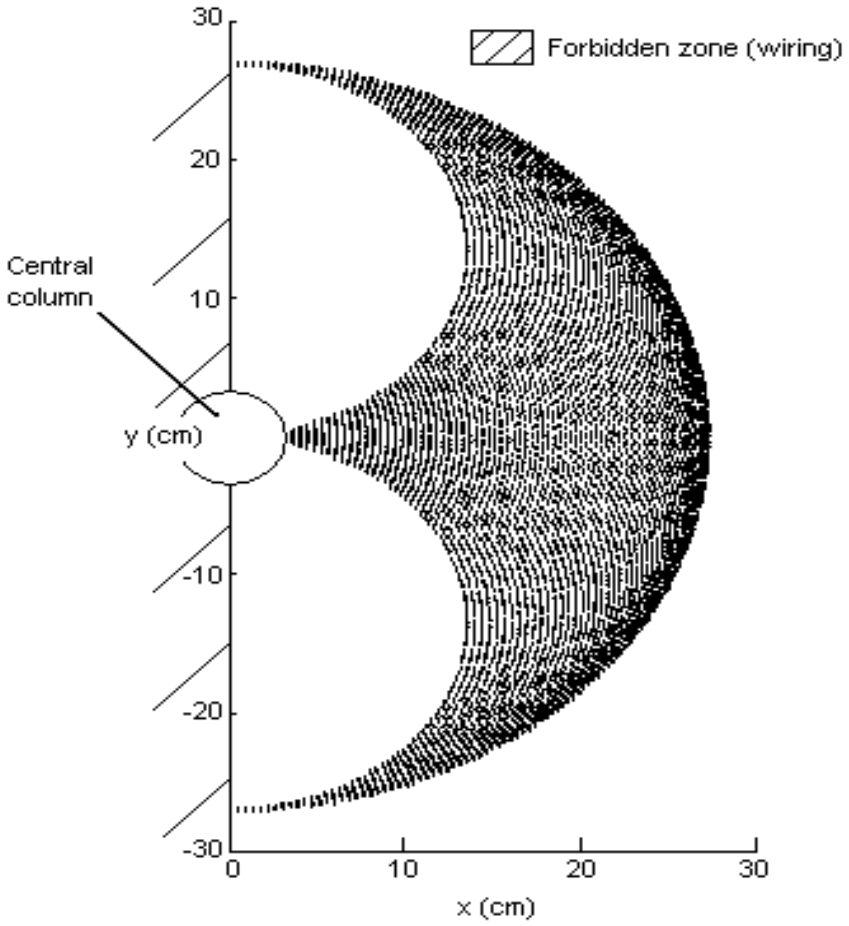

Figure 2.4: Tip workspace

3. COMPONENTS TESTING

In this chapter, we will evaluate the performance of the USM and the MPC. This evaluation is done with the components mounted on the device and the robot ready to use.

3.1 Ultrasonic Motor

3.1.1 Input-output characteristic

The aim of this subsection is to determine the DC voltage - rotational speed characteristic of the USM. To achieve this, various values of voltage are applied to the USM and the rotational speed is measured for each voltage value. As a consequence, we can plot the curve showing the DC voltage - rotational speed characteristic.

The characteristic is plotted in Figure 3.1. We can see that it is rather linear from minimum speed to maximum speed and that the behaviour is symmetric. There is a saturation effect at high speed, and the maximum speed measured is about 12.5 rad/s. Then, there is a large span of voltage (0 V to 0.5 V) on which the rotational speed of the USM will remain at its minimum speed, which is 2 rad/s.

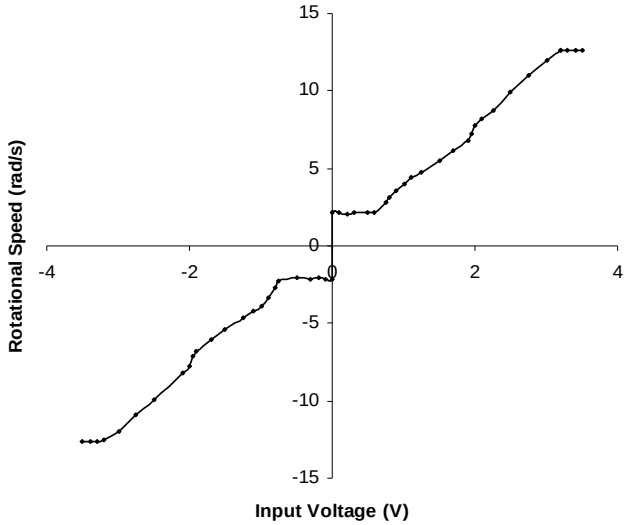

Figure 3.1: Rotational speed of the USM versus input voltage

3.1.2 Dynamic performance

This subsection deals with the response of the USM to step and sinusoidal inputs. During the experiments, the encoder signals were sampled at 1 kHz, and they were used to calculate the rotational speed of the motor. The rotational speed is derived from the encoder signals and filtered to remove the ripple. A digital PID controller is implemented as well, and the velocity is fedback to close the control loop. This control loop feedback mechanism will enable us to achieve better precision and wider bandwidth. The results presented further are obtained after a thorough tuning of the PID controller parameters.

The result of the USM's response to a step input is plotted in Figure 3.2. In this figure, the desired speed is 10 rad/s, which is a speed close to the maximum speed (12.5 rad/s). We can see that the response is quite fast as it requires less than 50 ms to reach the final speed value. The use of the feedback control loop ensures the precision of the scheme.

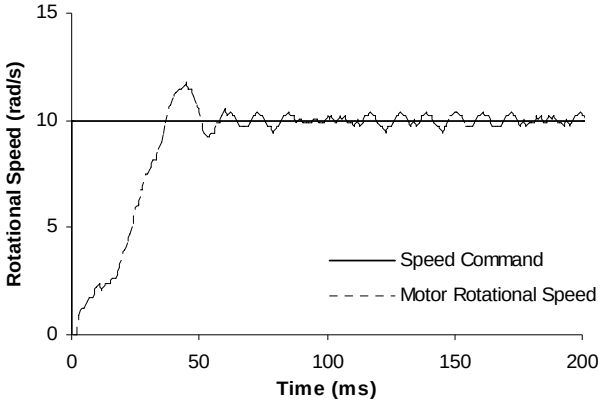

Figure 3.2: Speed response of the USM to a step command

The USM's response to sinusoidal inputs of different frequencies was tested. The 3dB-bandwidth was estimated at about 25 Hz. Figure 3.3 shows the Bode diagram in this case.

The main factor limiting the bandwidth is the 10 ms latency interval required when changing the direction of rotation.

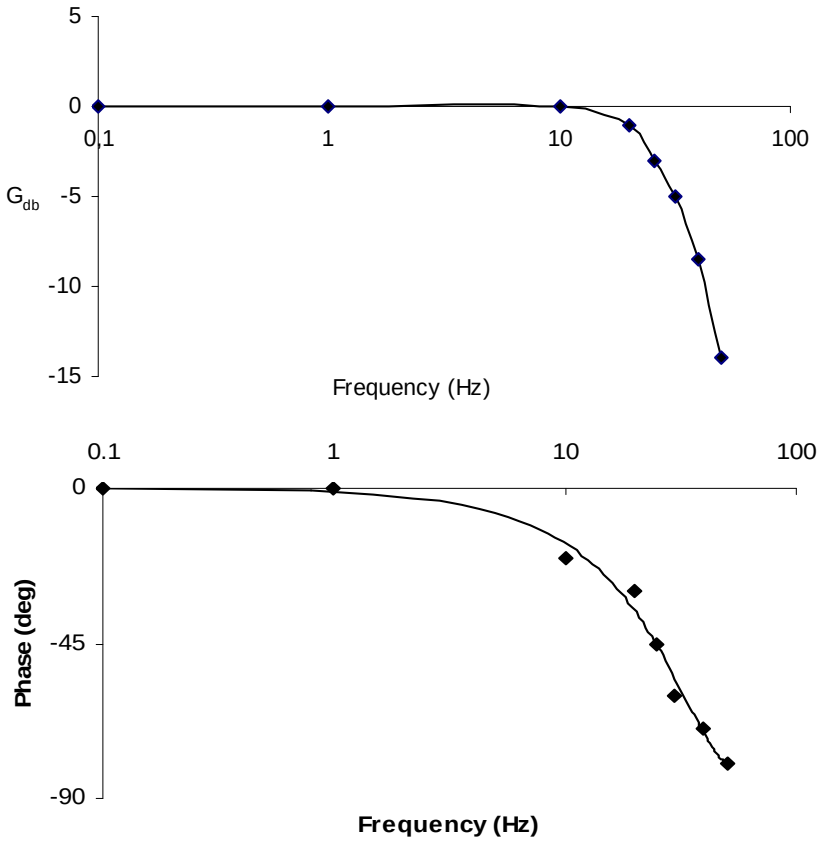

Figure 3.3: Bode diagram for USM speed response

In order to estimate the influence of this delay, other experiments were carried out without proceeding to a change in the direction of rotation. Therefore, an offset was added to the previous sinusoidal command so as to avoid zero crossing and the amplitude was not changed. This will ensure the consistency of the comparison. With this command, the bandwidth is found to be about 50 Hz, instead of the previous 25 Hz. Figure 3.4 shows a comparision between the speed responses with zero-crossing and without zero-crossing at a 25 Hz frequency.

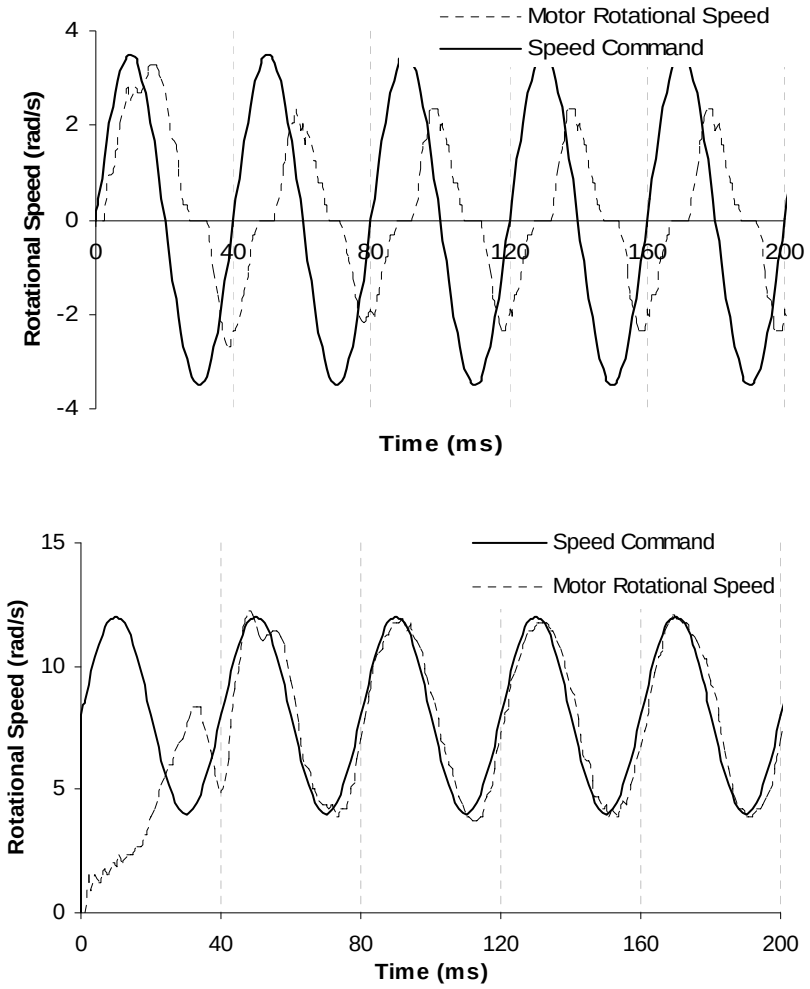

Figure 3.4: Speed response with zero-crossing (up), and without (down)

The USM's drawback seem to be due to the driver itself. Other research done on USM drivers [35, 37] using a phase difference control approach instead of a frequency control approach to drive the USM had the USM running without facing a minimal value for the USM rotational speed or any need of waiting 10 ms when changing the direction of rotation. Therefore with a more sophisticated driver, the experimental results show that we can expect a wider bandwidth.

3.2 Magnetic Particle Clutch

This section deals with the torque characteristics of the MPC. In the whole section, the USM will not be active. The output torque of the MPC will therefore be a resistive torque. As we do not have any torque sensors, we will measure the resistive force applied by the MPC to the first link of the arm. The resistive force can easily be measured with the force gauge placed at right angle to the link, and mounted with the appropriate implement, by the following formula: $\boldsymbol{F} = \frac{\tau}{\mathrm{L}}$. The resistive torque of the MPC can then be deduced. The setup is shown in Figure 3.5

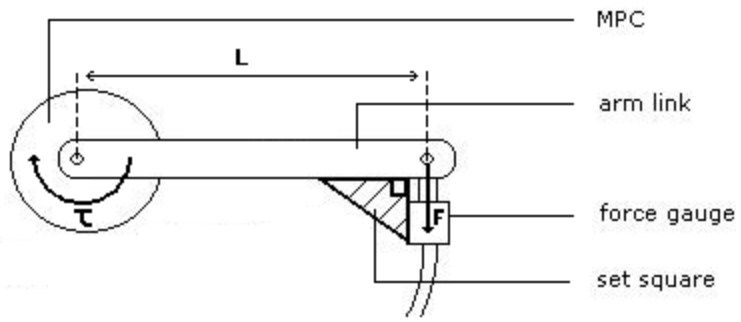

Figure 3.5: Torque measurement setup

3.2.1 Input-output characteristic

In this subsection, we will evaluate the current - torque profile of the MPC. The MPC's input current was increased from 0 to maximum and then decreased from maximum to 0. For each value of current, the resistive torque was measured. Figure 3.6 shows the current - torque curve of the MPC, which is a typical hysteresis curve. The hysteresis nature of the characteristic will affect the performance of the device.

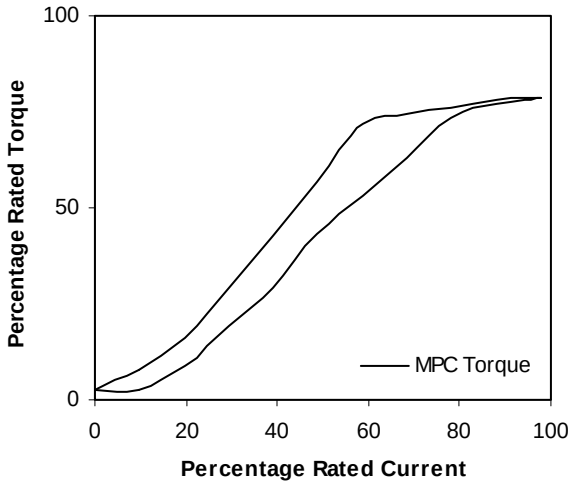

Figure 3.6: Current - torque characteristic of the MPC

The curve presents an S-shape as stated in the datasheet (Figure 2.3). However the saturation of the torque occurs earlier than expected. Indeed the force measured at the link corresponds to only 75% of the maximum torque of the MPC. Measurements done on the other MPC showed that only 65% of the torque was transmitted from the MPC to the link. This probably comes from the flexible coupling whose maximum torque is not high enough.

3.2.2 Dynamic performance

Here, we analyze the MPC response to step inputs. The maximum input value will stay within the range defined above. The output is the resistive torque transmitted by the MPC to the link.

Figure 3.7 shows the response to a step input. There is a response delay of about 30 ms, which was predictable as the datasheet informed us about this (unforced response 25 ms). Apart from that, the response is similar to a typical passive first order system. The main

observation is the slow settling time of the MPC, which will be the main limitation to the bandwidth.

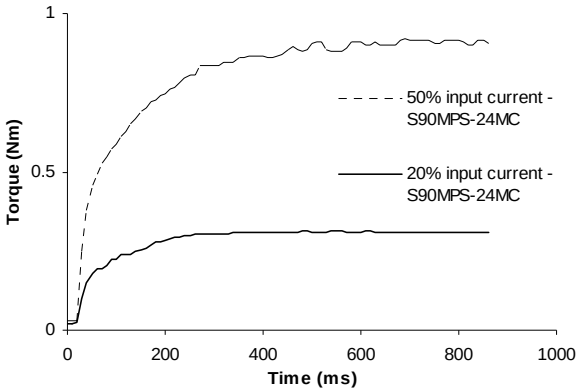

Figure 3.7: MPC response to torque step input

From the above observations, we can point out the following limiting factors. First, the hysteresis effect will reduce the performance of the interface, its precision in particular. Second, the nature of the rotational joint between the arm link and the output shaft of the MPC limits the torque transmission. Lastly, the MPC's settling time is slow, which reduces its bandwidth.

However, these drawbacks can be dealt with. The use of torque sensors to measure the torque at each link can improve the precision. The value of the torques can be fedback to the computer and used in a control loop, thus ensuring better precision. Provided a good tuning of control parameters, the response speed and the bandwidth can be improved as well. Better joints could improve the maximum transmitted torques from the MPC to the links.

3.3 Haptic device

In this subsection, we will mainly analyze the effect of the USM's minimum and maximum velocities on the performance of the haptic device. The speed ratio of a motor is defined to be the ratio of the minimum velocity of the motor to its maximum velocity. In the case of the USM, the ratio is 1:6.25. This low ratio will raise an issue on the velocity directions that can be given to the tip at certain positions. Indeed, the linear velocity is linked to the angular velocity by $\begin{pmatrix}\dot{\theta}_1\\ \dot{\theta}_2\end{pmatrix} = J^{-1}\cdot\begin{pmatrix}\dot{x}\\ \dot{y}\end{pmatrix}$. We will assume that J^{-1} is always defined, as the singular configurations will not occur because of the travel limitation and the mechanical stop. For the tip to follow a straight line, the ratio $\frac{\dot{y}}{\dot{x}}$ must be a constant, say $\mathrm{K}\in\Re$. That is,

$$\begin{pmatrix}\dot{\theta}_1\\ \dot{\theta}_2\end{pmatrix} = J^{-1}\cdot\begin{pmatrix}\dot{x}\\ \mathrm{K}\cdot\dot{x}\end{pmatrix} = \frac{1}{\mathrm{L}\cdot\sin(\theta_2-\theta_1)}\cdot\begin{pmatrix}\dot{x}\cdot(\mathrm{K}\cdot\cos(\theta_1)+\sin(\theta_1))\\ \dot{x}\cdot(-\mathrm{K}\cdot\cos(\theta_2)-\sin(\theta_2))\end{pmatrix}$$

This leads to the condition

$$\frac{\dot{\theta}_1}{\dot{\theta}_2} = -\frac{\mathrm{K}\cdot\cos(\theta_1)+\sin(\theta_1)}{\mathrm{K}\cdot\cos(\theta_2)+\sin(\theta_2)} \qquad (2)$$

for achieving a straight line.

For example, let us choose $\mathrm{K}=0$, which means the tip will move along $\vec{\mathrm{j}}$. In that case, (2) yields $\frac{\dot{\theta}_1}{\dot{\theta}_2} = -\frac{\sin(\theta_1)}{\sin(\theta_2)}$. Then $\left|\frac{\dot{\theta}_1}{\dot{\theta}_2}\right| \longrightarrow \infty$ when $\theta_2 \to 0$, (unless $\theta_1 \to 0$). The problem is that the maximum $\frac{\dot{\theta}_1}{\dot{\theta}_2}$ ratio based on our USMs is $\frac{12.5}{2}$, so when $\theta_2 \to 0$, it is

not always possible for the arm to move along $\vec{j}$. This example can be extended to any other directions. Therefore, in some configurations, directions which require big $\frac{\dot{\theta}_1}{\dot{\theta}_2}$ ratios cannot be followed.

Figure 3.8 contains some figures showing the possibility of achieving some velocity direction according to the position of the tip.

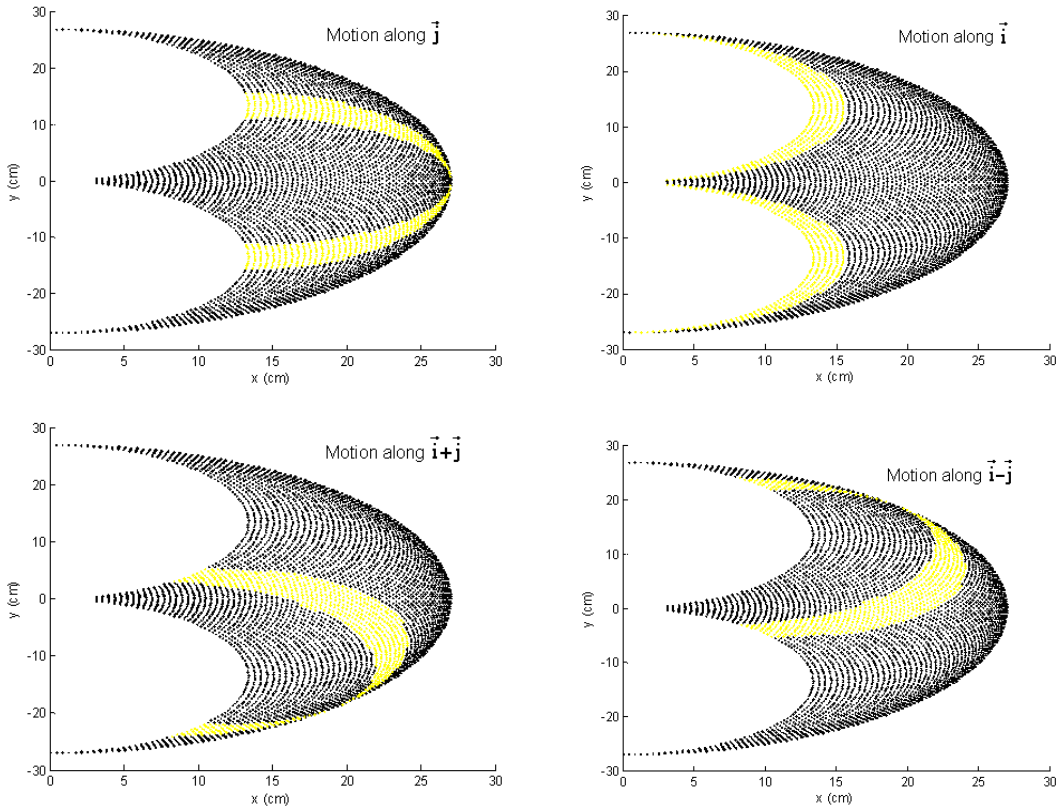

Figure 3.8: Achievable velocity directions (black) and non-achievable directions (yellow)

In spite of the good dynamic behaviour of the USMs, their use will from now on be restricted. They will be used for giving the direction of the force when rendering active force. The USM requiring the slower rotational speed will be set to its minimum speed, and the other USM's speed would be set according to (2).

4. HAPTIC INTERFACE EVALUATION

In this chapter, we will evaluate the performance of the interface. For that purpose, we will base our evaluation on the three necessary criteria for an effective interface by Massie and Salisbury [33] when they tested the Phantom® device. The data resulting from these criteria can usually be found in the specifications of haptic interfaces. In addition, we will also present other data and experiment results to give a deeper evaluation of the performance of our interface.

4.1 Evaluation according to the three necessary criteria

4.1.1 Free space must feel free

This is the first criterion. When free space is simulated, the interface must not affect the user. Ideally the user should not feel the resistance. It results in the following requirements: little backdrive friction and low inertia.

The friction is the lowest when the MPCs are not excited. In that situation, the resistive force at the tip of the arm is the backdrive friction. The resistive force depends on the configuration of the arm (see appendix for more details). We will consider as relevant for our interface the results we find when the links of the arm are orthogonal, and the tip is placed on the x axis. The user will be mostly moving around this position. The position of the tip in this configuration will be called the nominal position. Measurements performed with the force gauge showed that the backdrive friction is about 0.4 N in nominal position.

We now have to evaluate the inertia of the arm. The nature and geometry of the links of the arm were chosen such that they would have low inertia. To estimate the inertia of the device, we have to measure the value of the inertia parameters in the dynamics of the

system. Details on predictions, experimental results and apparent mass calculation are given in the appendix. Predictions gave inertia values of $4 \cdot 10^{-4}\,\mathrm{kg.m^2}$ and $8 \cdot 10^{-4}\,\mathrm{kg.m^2}$ for the different parameters. Results gave $6 \cdot 10^{-4}\,\mathrm{kg.m^2}$ and $1 \cdot 10^{-3}\,\mathrm{kg.m^2}$ .The results are larger than predicted because the predictions did not take into account the influence of the rotational joints between the links. The resulting apparent mass of the interface in nominal position is 15 g in the x direction and 45 g in the y direction.

4.1.2 Solid virtual objects must feel stiff

The aim of this subsection is to estimate the maximum stiffness achievable while the interface remains stable. Stiffness is the resistance of an elastic body to deformation by an applied force. Assuming a linear model, it links the force to the deformation by $\vec{F} = \mathrm{k} \cdot \vec{d}$, where k is the stiffness of the body and *d* the penetration within it. Once the body is deformed, it will react by applying a force in the opposite direction of its deformation. Therefore the force rendering stiffness is active, and will require the use of the motors.

The torque of the MPCs will be given according to $\boldsymbol{\tau} = \boldsymbol{J}^T \cdot \boldsymbol{F}$, with $\boldsymbol{F} = \mathrm{k} \cdot \boldsymbol{d}$, while the direction of the force will be set by the USMs. The body will be placed such that the contact with the tip will occur around the nominal position.

The estimation of the maximum stiffness achievable is difficult, as it is a subjective criterion [29]. In our case, the user will hold the tip of the arm with his fingers and will move the tip towards a virtual wall modeled as a spring with high stiffness. When the user is in contact with the virtual wall, he will either feel comfortable or feel oscillations. The maximum stiffness occurs before the user feels any oscillations. For each user, the stiffness was increased till he felt oscillations. For our interface, four different users were

asked to perform the experiment, and we evaluated the maximum stiffness at 15000 N/m. Under this value, every users felt comfortable. Figure 4.1 shows the position of the tip when going towards contact with the wall, when the stiffness simulated is 15000 N/m, for one random user. We can notice that the trajectory of the tip is close to a straight line during the whole course of the contact.

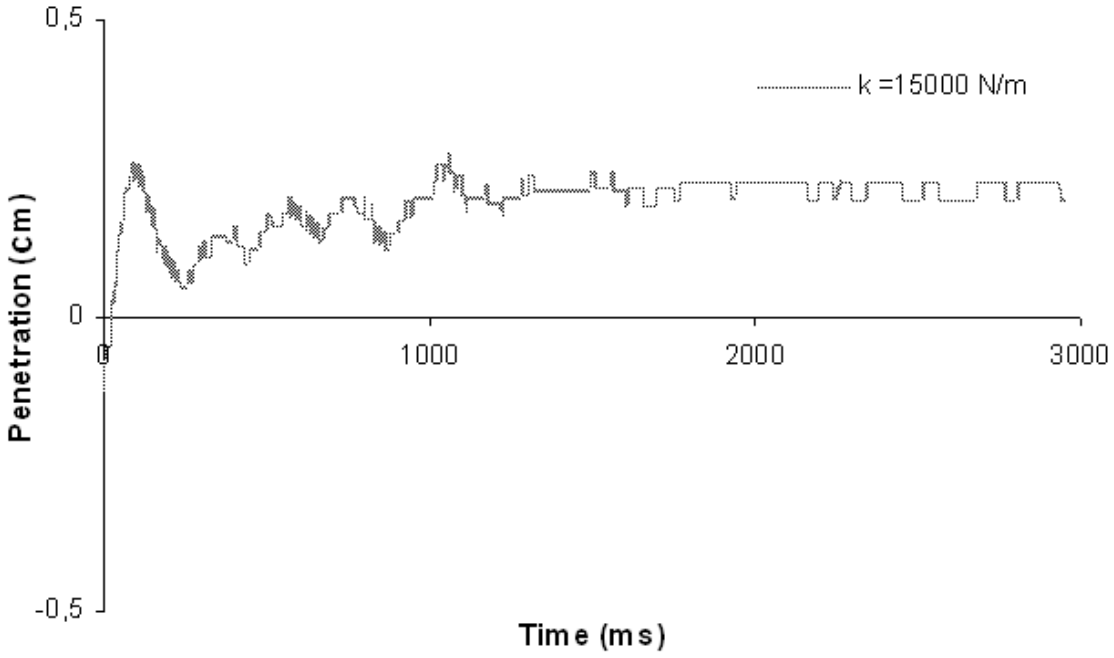

Figure 4.1: Maximum achievable stiffness

4.1.3 Virtual constraints must not be easily saturated

A haptic interface must be able to resist the force applied by the user. If a wall is simulated, the user must not be able to go through the wall. In order to estimate the force capability of our interface, we measured its maximum peak force and its maximum continuous force. These forces were measured with the tip placed at the nominal position. The values will vary according to the nature of the force. We will therefore differentiate the cases of active force and passive force.

For active forces, the maximum peak force was measured as follows. The MPCs torque is set to their maximum allowed value (60% of rated torque). Then the USMs are turned on, and the force gauge measures the force at the tip. Therefore the force measured is an active force. It is the maximum peak force as the motors cannot maintain this force and will stop due to overloading. Measurements gave 6.5 N.

A similar strategy was followed to determine the maximum active continuous force. We adjusted the value of the MPCs torque to the USMs rated torque, and we let the USMs run continuously for one minute. The maximum continuous force measured was 3.2 N.

In passive mode, different values were found. Our interface enables us to simulate resistive forces such as viscous damping or Coulomb friction without requiring the USMs. The MPCs alone can simulate these forces. The resulting forces will be passive, stable and safe for the user. To measure the maximum forces, the MPCs torque was set to their maximum allowed value (60% of rated torque). The maximum peak force and the maximum continuous force were both 6.5 N.

4.1.4 Comparison with other interfaces

The most common haptic interfaces we can find are the ones from the Phantom® series. They are quite similar to our device in terms of workspace (considering two dimensions) and size. Therefore we will use two models of the Phantom® series as reference for comparison purposes. We will also compare our device to another popular desktop interface, the Omega.3, which is a parallel device as opposed to the Phantom® which is a serial device. The Phantom® and Omega.3 interfaces use DC motors as actuators, Omega.3 using more powerful motors then the Phantom®.

Table 4.1 draws the comparison for the different parameters estimated above [41, 42, 43, 44].

Table 4.1: Interfaces comparison

	Our interface	Omega.3	Phantom® Desktop™	Phantom® Omni™
Backdrive Friction	0.4 N	0.15 N	0.06 N	0.26 N
Apparent mass at the tip	45 g	220 g	45 g	45 g
Maximum Stiffness	15000 Nm	14500 Nm	2350 Nm	1340 Nm
Maximum Force (Nominal Position)	6.5 N	12 N	7.9 N	3.3 N
Continuous Force (Nominal Position)	3.2 N	12 N	1.75 N	0.88 N

We can see that apart from the backdrive friction, the interface has quite good results. Our interface has a higher backdrive friction than other interfaces. This is merely due to the backdrive torque of the MPC. The apparent mass at the tip is similar to the Phantom® devices while the Omega.3's is much higher, as it uses more powerful motors which cause more inertia. However a direct comparison can not be relevant as other devices have more DOF, therefore more links and more inertia involved. However it shows that the inertia of our interface is good.

As for the maximum stiffness, the interface shows good improvements compared to Phantom® devices. Indeed our interface can simulate stiffness 6 times greater than the Phantom® Desktop™ 1.0 and 10 times greater than the Phantom® Omni™. The

interface's maximum stiffness is about the same as the Omega.3**.** For the Omega.3, the high maximum stiffness is due to its parallel structure and the use of more powerful motors, what increases inertia, thus stiffness. Our interface has a high stiffness while keeping a low inertia. There are mainly two explanations for that. First, the use of the MPCs as natural dissipative elements helps the interface to absorb the extra energy from the USMs and the user, thus improving the interface stability. Second, the parallel structure also helps increasing stiffness.

Lastly, we see that the active force characteristics of our interface are good. The maximum force is slightly lower than the Phantom® Desktop™ and the Phantom® Premium™ and the continuous force is much higher than for other Phantom® devices. This is due to the use of USM, which has higher rated torque than common electric motors at equal size. When simulating passive forces, the advantage of using the MPC is even greater as it can continuously simulate a force of 6.5 N. The Omega.3 is obviously more powerful than all other interfaces.

From these comparisions, we can see that our haptic interface fullfills the three necessary criteria and has significantly good results for criterion (2).

4.2 Force bandwidth

Here we estimate the force bandwidth of the arm. The arm will be subjected to force commands. The force will be an active force produced by the USMs and will be measured at the tip of the arm by the force gauge. The experiments were carried out in different configurations of the arm.

First, the response of the tip to a force step input is investigated. At first, the MPCs are not excited. Once the USMs are running, a step command is sent to the MPCs. This will result in a force step input. Figure 4.2 shows the force response of the tip to a force step input at nominal position. We notice that the settling time is quite slow. This is due to the MPCs who have a low settling time as we saw before.

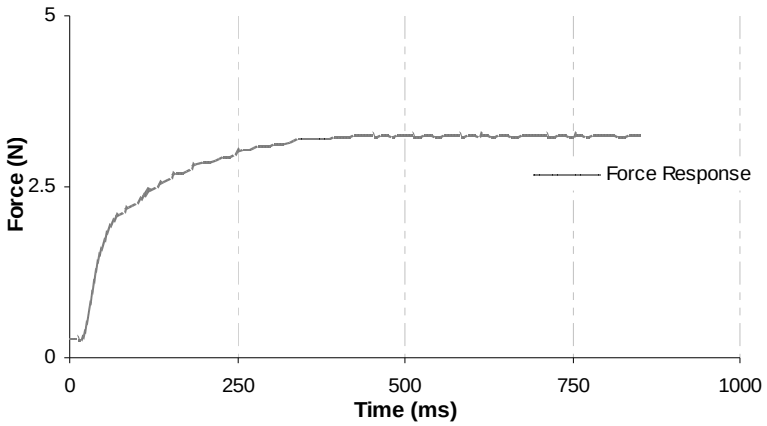

Figure 4.2: Response of the tip to a force step input

Then the response to sinusoidal inputs is investigated. This time, the MPCs are excited at the beginning. The reason of this excitation is to give an offset value to the sinusoidal command. When the USMs start running, a sinusoidal command is sent to the MPCs. The 3dB-bandwidth could then be measured. We found a bandwidth around 2 Hz. Figure 4.3 shows the frequency response of the tip where $\frac{F}{F_d}$ is the ratio of measured force to desired force.

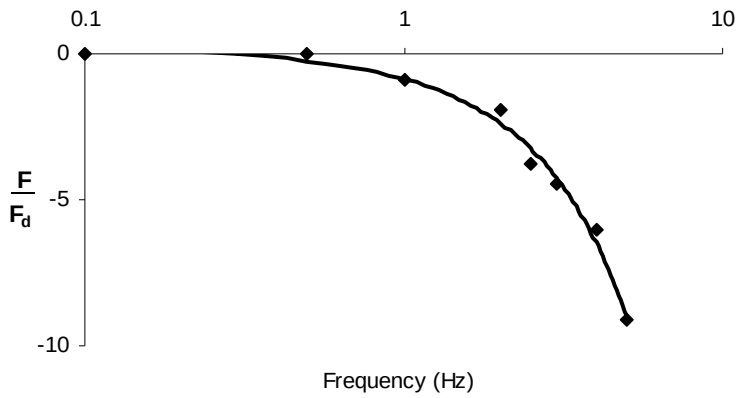

Figure 4.3: Magnitude Bode diagram

This force bandwidth is narrow because of the slow responsiveness of the MPCs. [46] and [47] claimed to have achieved over 100 Hz and 48 Hz respectively. However Brooks [39] showed that the human operator's perceivable bandwidth is 5.6 Hz on average. The use of force sensors for feedback will probably increase the bandwidth enough to exceed this value.

4.3 Force-field simulation

Here we will use our haptic interface for simulating different force-fields that were taken into account in other studies as additional criteria. Experiments were made involving three other users. For each force-field simulated, they would give their feeling on the interaction.

4.3.1 Free space

When free space is simulated, the user must not feel any resistive force. The first step to achieve good free motion experience comes from the mechanical design. The interface's inertia should be low and its backdrive friction little. In our interface, we saw that these

parameters were acceptable compared to other devices. Therefore, the user does not really feel restricted when he moves.

In order to improve the free feeling, we tried to help the user in his motion by using the USMs during the free space simulation. The USMs were set to their minimal rotational speed (2 rad/s), and the MPCs were not excited, thus their resistive torque remained to their backdrive friction torque. Therefore the tip is driven at the backdrive friction force during its motion. The sense of rotation given to the links by the user manipulating the tip is tracked by the encoders. The USMs will be commanded such that their sense of rotation is the same as the links they actuate. In fact, the interface will help the user in his motion by providing a low force at a low speed. As the MPCs are placed between the arm and the USMs, they will ensure the force is constantly minimal, regardless of the USMs' torque. We hope this strategy will improve the user's free motion sensations.

It is quite difficult to find a relevant way to illustrate the efficiency of a strategy for free motion as it is mainly based on feeling. We tested the strategy on three users. After giving some time to them to familiarize with the interface until they felt comfortable with it, they were asked to follow different paths without the help of the USM. After that, they were asked to familiarize with the haptic inteface's behaviour with the help of the USMs. And asked to move again along the same paths. In both situations, their trajectories along the paths were recorded. Results for a straight path are shown in Figure 4.4. We can notice that the trajectories are smoother with the help of the USMs. Moreover, the user is also able to move faster and doesn't feel any opposition. However in paths involving a change of direction, users complained about an odd behaviour as the motors were changing direction.

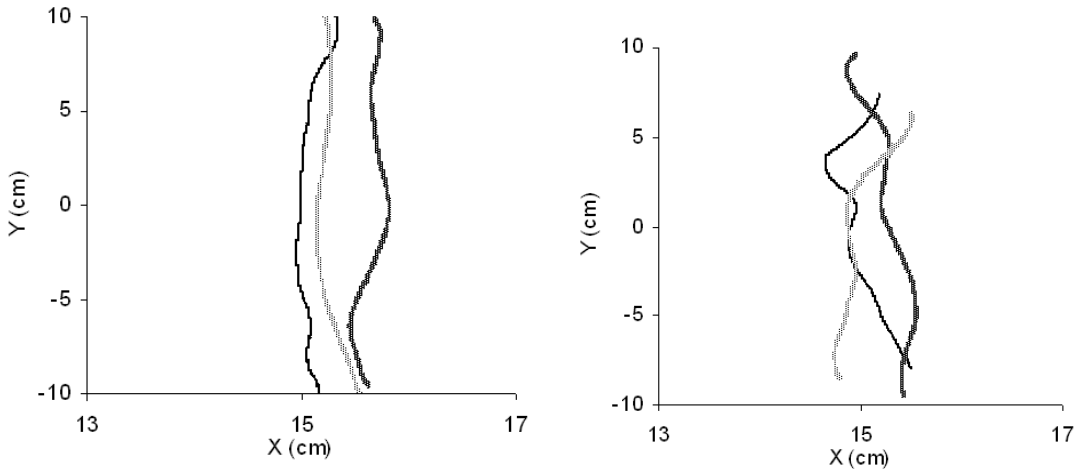

Figure 4.4: Trajectory of the tip when the user tries to follow a straight path with the help of the USM (left) and without (right)

4.3.2 Wall

Wall simulation is a common test to evaluate the quality of a haptic interface [45, 47, 48]. This test gives an idea on the performance of stiffness simulation and on the responsiveness of the interface. In our experiments, the walls were simulated by adding stiffness to them. According to [33], the user is convinced he is facing an unmovable wall for a certain stiffness value, lower than the maximum stiffness. Reducing stiffness offers a better stability when the speed impact is high and the force is strong. For determining the stiffness used for simulating the wall, we had to find a compromise between hard stop and good stability. This value depends on many factors as pointed out in [49].

In our experiments, the torque of the MPCs will be given according to $\boldsymbol{\tau} = \boldsymbol{J}^T \cdot \boldsymbol{F}$, with $\boldsymbol{F} = \mathrm{k} \cdot \boldsymbol{d}$, while the direction of the force will be set by the USMs. After trying different stiffness values, we fixed the stiffness value k to 2000 N/m and let the three users interact with the wall. They agreed they felt stopped by the wall and could move smoothly along

the wall. However when they felt in contact with the wall, they had already penetrated and gone beyond the wall, because of the slow force response of the interface. Figure 4.5 shows how fast the velocity decreases when the tip reaches the wall and Figure 4.6 shows the penetration of the tip in the wall and the motion along it, in the case of one random user.

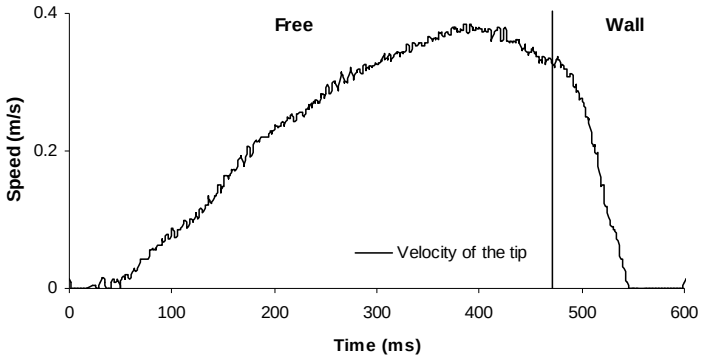

Figure 4.5: Velocity of the tip before and after encounter with the wall

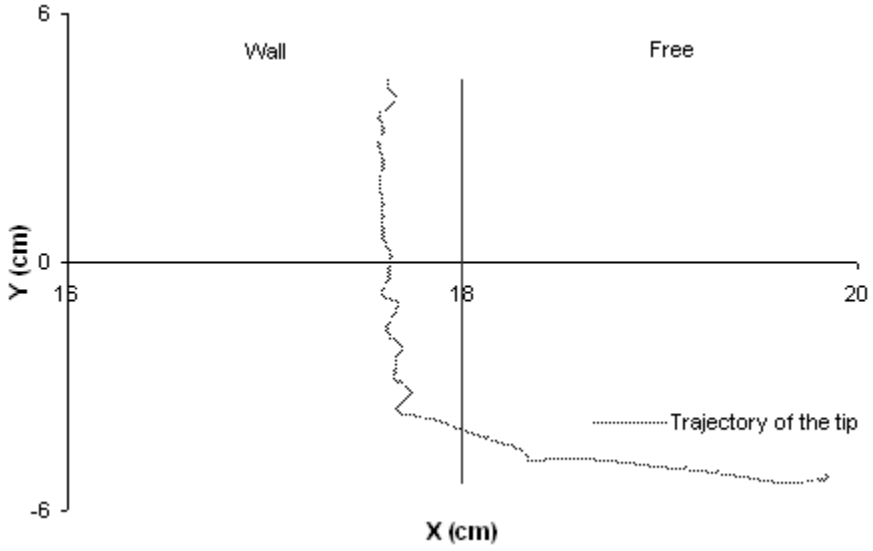

Figure 4.6: Wall simulation with stiffness of 2000 N/m

4.3.3 Coulomb friction

Friction is the force resisting the relative motion of two surfaces in contact. It occurs for example when someone is pushing a crate on the floor. The resistive force of the floor on

the crate will be constant and opposed to the movement direction. Jex [47] considered the simulation of Coulomb friction as a critical test in addition to the three necessary criteria. Unlike active interfaces, our hybrid interface can naturally provide stable passive force simulation due to the presence of the MPCs. To simulate Coulomb friction, we give a force step input to the MPCs when the user comes into contact with the item he has to push, and we maintain it while he is pushing. Once he stops pushing, the force input is set back to 0. Three different users tried to push the virtual crate.

Figure 4.7 shows the simulation of Coulomb friction occurring in nominal position for a random user. At first the user moves freely towards the item he will have to push, then he will push the item, and lastly he will stop pushing and will move away from the item.

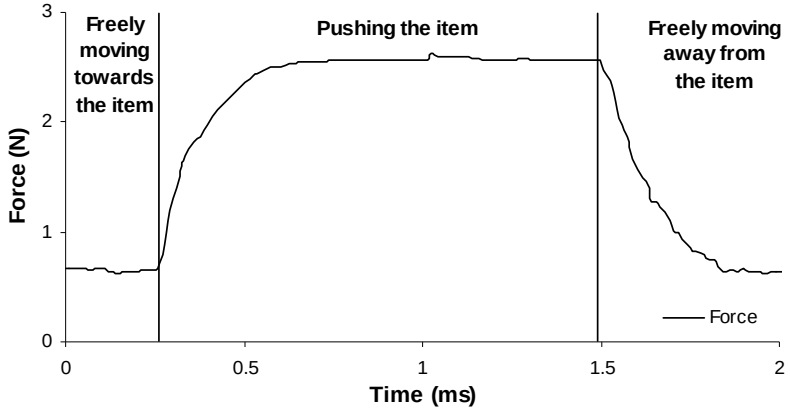

Figure 4.7: Simulation of friction

Results proved to be really good. The force remained more or less constant throughout the pushing, once it had reached its constant value. Users really felt the constant resistance. Contrary to active interfaces, the movement is perfectly stable as only the passive MPCs are working, and users are comfortable when alternating between pushing and "resting". However, it takes some time to reach the final force value.

5. CONCLUSION AND FUTURE RESEARCH

A general purpose two-DOF haptic device was developed for interacting with virtual environments. It was compared with other common devices and tested through the implementation of several force-fields. Its originality lies in the nature of its actuators. Instead of the usual active actuators, the actuators are hybrid actuators, composed of an active actuator, the ultrasonic motor, and a passive actuator, the magnetic particle clutch. The haptic interface proved to be an efficient interface with augmented stability and good simulation capabilities.

USMs proved to be a good alternative to conventional electromagnetic motors. It has low inertia, compactness and good dynamic capabilities, and its continuous force is much higher, hence stronger forces can be simulated continuously. However it also has several drawbacks, the most important being its low speed ratio.

The use of MPCs improved the stability to the interface. The passive force fields simulated here are naturally stable, contrary to those based on active interfaces. It also brought better stiffness capabilities to the user, thus giving better simulating capabilities for active force fields. However it is also the limiting factor of the interface as its low force-bandwidth limits the responsiveness of the interface and its hysteresis reduces its precision.

In the future, an important improvement that can be made is the use of torque sensors for feedback. It can increase the bandwidth and the precision of the MPC, thus improving the force response. Improvements in USM drivers will allow an increase of the speed ratio and of the bandwidth by reducing the latency when changing the direction of rotation.

Bibliography

[1] I. Hunter et al. Ophthalmic microsurgical robot and surgical simulator. Proceedings of SPIE , Vol. 2351, pp. 184-90, Telemanipulator and Telepresence Technologies, 1994.

[2] H. Kazerooni. Human enhancement via the transfer of power and information signals. Engineering Advances: New Opportunities for Biomedical Engineers. Proceedings of the 16th Annual International Conference of the IEEE, Vol. 2, pp. 1057-1058, 3-6 November 1994.

[3] N. Hogan, B. A. Kay, E.D. Fasse, F.A. Mussa-Ivaldi. Haptic illusions: experiments on human manipulation and perception of virtual objects. Cold Spring Harbor Symposia on Quantitative Biology, Vol. 55, pp. 925-93, 1990.

[4] G. Robles-De-La-Torre, V. Hayward. Virtual surfaces and haptic shape perception. Proceedings of the Haptic Interfaces for Virtual Environment and Teleoperator Systems Symposium, ASME IMECE 2000, Orlando, Florida, USA, Vol. 69; No. 2, pp. 1081-7, 2000.

[5] R.M. Satava. Virtual reality surgical simulator: the first steps. Surgical Endoscopy, pp.203-205, July. 1993.

[6] M. Bergamasco, B. Allota, L. Bisio, L. Ferretti, G. Parini, G.M. Prisco, F. Salsedo, G. Sartini. An arm exoskeleton system for teleoperation and virtual environments applications. Proceedings of the IEEE International Conference on Robotics and Automation, pp. 1449-54, 2000.

[7] www.hocoma.ch

[8] home.novint.com

[9] www.sensable.com

[10] www.forcedimension.com

[11] www.haption.com

[12] www.immersion.com

[13] www.mpb-technologies.ca

[14] J.E. Colgate, P.E. Grafing, M.C. Stanley, G. Schenkel. Implementation of stiff virtual walls in force-reflecting interfaces. IEEE Virtual Reality Annual International Symposium, Seattle, WA, pp. 202-207, 1993.

[15]N. Hogan. Controlling impedance at the man/machine interface. Proceedings of the IEEE International Conference on Robotics and Automation, pp. 1626-1631, 1989.

[16] B. Gillespie, M. Cutkosky. Stable user-specific rendering of the virtual wall. ASME IMECE, Atlanta, GA, Vol. DSC-Vol. 58, pp. 397-406, 1996.

[17] R. Ellis, N. Sarkar, M. Jenkins. Numerical methods for the force reflection of contact. ASME Journal of Dynamic Systems, Measurement and Control, Vol. 119, pp. 768-774, 1997.

[18] B. Hannaford, J.H. Ryu. Time domain passivity control of haptic interfaces. Proceedings of the IEEE International Conference on Robotics and Automation, pp. 1863-1869, 2001.

[19] S.Stramigioli, C.Secchi, A. Van Der Schaft, C. Fantuzzi. A novel theory for sample data system passivity. Proceedings of the IEEE/RSJ International Conference on Intelligent Robots and Systems, Lausanne, Switzerland, 2002.

[20] J. J. Abbott, A. M. Okamura. Effects of position quantization and sampling rate on virtual-wall passivity. IEEE Transactions on Robotics, No. 5, Vol. 21, pp. 952-964, 2005.

[21] W. Townsend, J. Salisbury. The effect of coulomb friction and stiction on force control. Proceedings of the IEEE International Conference on Robotics and Automation, pp. 883-889, 1987.

[22] M. Mahvash, V. Hayward. High fidelity passive force reflecting virtual environments. IEEE Transactions on Robotics, No 1, Vol. 21, pp. 38-46, 2004.

[23] S. Zhai, P. Milgram, W Buxton. The influence of muscle groups on performance of multiple degree-of freedom input. Proceedings of CHI 96, pp. 308-315, 1996.

[24] D.K. Pai, E.W. Van Der Loo, S. Sadhukhan, P.G. Cry. The Tango: a tangible tangoreceptive whole-hand human interface. Symposium on Haptic Interfaces for Virtual Environment and Teleoperator Systems 2005, pp 141- 147, 2005.

[25] D. K. Swanson, W. J. Book. Obstacle avoidance methods for a passive haptic display. Proceedings of the IEEE International Conference on Advanced Intelligent Mechatronics, pp. 1187-1192, 2001.

[26] K. Koyanagi, J. Furusho, L. Dong. Study on force display system using redundant couple of ER brakes. Proceedings of the IEEERSJ International Conference on Intelligent Robots and Systems, Sendai, Japan, pp. 3251-3256, 2004.

[27] J. An, D.S. Kwon. Haptic experimentation on a hybrid active/passive force feedback device. Proceedings of the 2002 IEEE International Conference on Robotics & Automation, Washington DC, May 2002.

[28] M. Russo, A. Tadros. Controlling dissipative magnetic particle brakes in force reflecting devices. Proceedings of the ASME Winter Annual Meeting, Anaheim, California, pp. 63-70, 1992.

[29] J. E. Colgate, J. M. Brown. Factors affecting the Z-width of a haptic display. Proceedings of the IEEE International Conference on Robotics and Automation, San Diego, CA, Vol. 4, pp. 3205-3210, 1994.

[30] E. Ruffaldi, D. Morris, T. Edmunds, F. Barbagli, D.K. Pai. Standardized evaluation of haptic rendering systems. Proceedings of IEEE Haptic Symposium, pp. 225-232, 2006.

[31] R. Ellis, O. Ismaeil, M. Lipsett. Design and evaluation of a high-performance haptic interface. Robotica, 1996.

[32] D.A. Lawrence, L.Y. Pao, A.M. Dougherty, M.A. Salada, Y. Pavlov. Rate-hardness: a new performance metric for haptic interfaces. IEEE Transactions on Robotics and Automation, Vol. 16, pp. 357-371, 2000.

[33] T.H. Massie, J.K. Salisbury. The phantom interface: a device for probing virtual objects. Proceedings of ASME Winter Annual Meeting, Symposium on Haptic Interfaces for a Virtual Environment and Teleoperator Systems, 1994.

[34] T. Sashida, T. Kenjo. An Introduction to Ultrasonic Motors. Oxford, Clarendon Press, 1993.

[35] N. Bigdeli, M. Haeri. Modeling of an ultrasonic motor based on Hammerstein model structure. 8th International Conference on Control, Automation, Robotics and Vision, Kumming, China, 6-9 December 2004.

[36] Shinsei website, www.shinsei-motor.com.

[37] F. Giraud, B. Semail, J.T. Audren. Analysis and phase control of a piezoelectric traveling-wave ultrasonic motor for haptic stick application. IEEE Transactions on Industry Applications, Vol. 40, pp. 1541-1549, 2004.

[38] Sterling Instuments catalog.

[39] T.L. Brooks. Telerobotic response requirements. Proceedings of IEEE International Conference on Systems, Man, and Cybernetics, Los Angeles, CA, pp. 113-120, 1990.

[40] Servo To Go, Windows Driver Software Manual.

[41] SensAble Technologies, Specifications for the PHANTOM® Desktop™ and PHANTOM® Omni™ haptic devices.

[42] SensAble Technologies, Specifications comparison for the PHANTOM® Premium™.

[43] Force Dimension, Omega haptic device brochure

[44] N. Diolaiti, G. Niemeyer, F. Barbagli, J.K Salisbury. Stability of haptic rendering: discretization, quantization, time-delay and coulomb effects. IEEE Transactions on Robotics, Vol. 22, Issue 2, pp. 256-268, 2006

[45] R.D. Howe. Force-reflecting teleoperated hand system for the study of tactile sensing in precision manipulation. Proceedings of the IEEE International Conference on Robotics and Automation, pp.1321-1326, 1992

[46] B.D. Adelstein, M.J. Rosen. Design and implementation of a force-reflecting manipulandum for manual control research. Advances in Robotics, ASME DSC Vol. 42, pp. 1-12, 1992.

[47] H. Jex. Four critical tests for control-free simulators. 23rd Annual Conference on Manual Control, Cambridge, Massachusetts, 1988.

[48] M. Arcy. Design of a single degree of freedom mechanical breadboard haptic display. Master of science thesis, Northwestern University, 1996.

[49] H.Z. Tan, B. Eberman, M.A. Srinivasan, B. Cheng. Human factors for the design of force-reflecting haptic interfaces. Dynamic Systems and Control, Vol. 55-1, 1994.

Appendix: Arm Model

Dynamic model

For deriving the dynamic equations of the arm, we will make the following assumptions:

(1) The system will be considered as a symmetric planar system.

(2) The joints and links are considered perfect: they totally transmit torque and motion with no friction, no stiffness and no backlash.

(3) The gravitational effects can be neglected.

(4) The density throughout the links is constant.

Let θ_1 and θ_2 be the coordinates mapping the first two links of the system, and Q_1 and Q_2 the moments associated. Under (1), let L be the length of each link, m its mass and I its inertia along z axis.

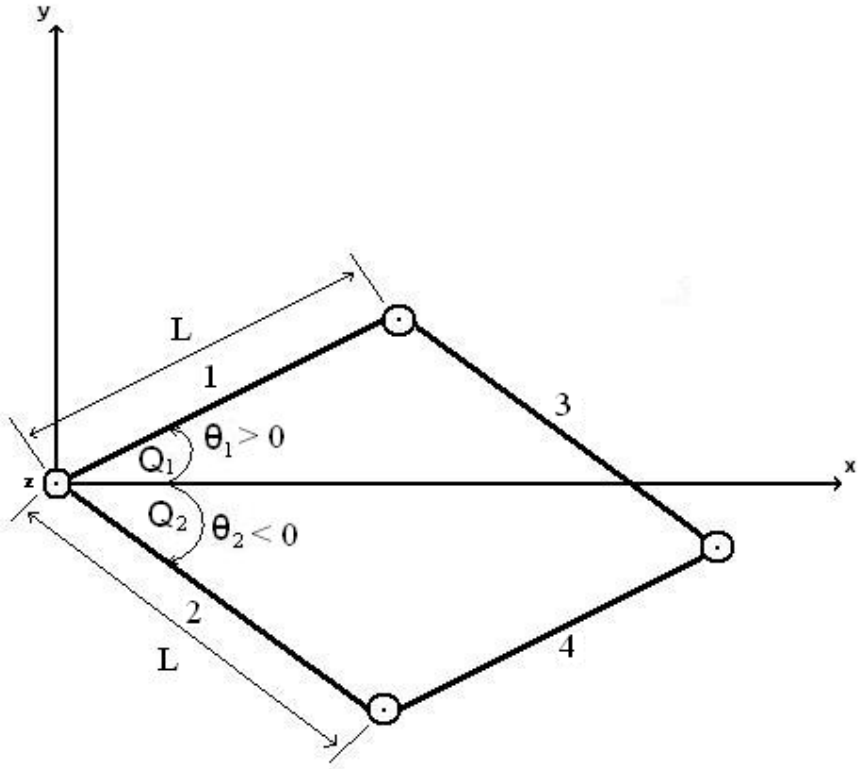

Figure A.1: Coordinates and moments definition

First, let us calculate the kinetic energy K_i of link i:

$$K_1 = \frac{1}{2} \cdot \mathrm{m} \cdot \left(\frac{\mathrm{L}}{2} \cdot \dot{\theta}_1 \right)^2 + \frac{1}{2} \cdot \mathrm{I} \cdot \left(\dot{\theta}_1 \right)^2$$

$$K_2 = \frac{1}{2} \cdot \mathrm{m} \cdot \left(\frac{\mathrm{L}}{2} \cdot \dot{\theta}_2 \right)^2 + \frac{1}{2} \cdot \mathrm{I} \cdot \left(\dot{\theta}_2 \right)^2$$

For link 3, we have to find the velocity of its centre of mass. Therefore, we first derive its position.

$$\begin{pmatrix} x_3 \\ y_3 \end{pmatrix} = \begin{pmatrix} \mathrm{L} \cdot \cos(\theta_1) + \frac{\mathrm{L}}{2} \cdot \cos(\theta_2) \\ \mathrm{L} \cdot \sin(\theta_1) + \frac{\mathrm{L}}{2} \cdot \sin(\theta_2) \end{pmatrix}$$

Then we get the velocity by derivation,

$$\begin{pmatrix} \dot{x}_3 \\ \dot{y}_3 \end{pmatrix} = \begin{pmatrix} -\dot{\theta}_1 \cdot \mathrm{L} \cdot \sin(\theta_1) - \dot{\theta}_2 \cdot \frac{\mathrm{L}}{2} \cdot \sin(\theta_2) \\ \dot{\theta}_1 \cdot \mathrm{L} \cdot \cos(\theta_1) + \dot{\theta}_2 \cdot \frac{\mathrm{L}}{2} \cdot \cos(\theta_2) \end{pmatrix}$$

and we deduce the squared amplitude of the velocity

$$V_3^{\,2} = \left(\dot{\theta}_1 \cdot \mathrm{L} \right)^2 + \left(\dot{\theta}_2 \cdot \frac{\mathrm{L}}{2} \right)^2 + \mathrm{L}^2 \cdot \dot{\theta}_1 \cdot \dot{\theta}_2 \cos(\theta_2 - \theta_1)$$

Lastly, we have the kinetic energy of link 3:

$$K_3 = \frac{1}{2} \cdot \mathrm{m} \cdot \left(\left(\dot{\theta}_1 \cdot \mathrm{L} \right)^2 + \left(\dot{\theta}_2 \cdot \frac{\mathrm{L}}{2} \right)^2 + \mathrm{L}^2 \cdot \dot{\theta}_1 \cdot \dot{\theta}_2 \cos(\theta_2 - \theta_1) \right) + \frac{1}{2} \cdot \mathrm{I} \cdot \left(\dot{\theta}_1 \right)^2$$

By symmetry we can deduce the kinetic energy of link 4:

$$K_4 = \frac{1}{2} \cdot \mathrm{m} \cdot \left(\left(\dot{\theta}_2 \cdot \mathrm{L} \right)^2 + \left(\dot{\theta}_1 \cdot \frac{\mathrm{L}}{2} \right)^2 + \mathrm{L}^2 \cdot \dot{\theta}_1 \cdot \dot{\theta}_2 \cos(\theta_2 - \theta_1) \right) + \frac{1}{2} \cdot \mathrm{I} \cdot \left(\dot{\theta}_2 \right)^2$$

Therefore the total kinetic energy of the system is

$$K = K_1 + K_2 + K_3 + K_4$$
$$K = \left(\mathrm{I} + \frac{3}{4}\cdot \mathrm{m}\cdot \mathrm{L}^2\right)\cdot \dot{\theta}_1 + \left(\mathrm{I} + \frac{3}{4}\cdot \mathrm{m}\cdot \mathrm{L}^2\right)\cdot \dot{\theta}_2 + \mathrm{m}\cdot \mathrm{L}^2\cdot \cos(\theta_2 - \theta_1)\cdot \dot{\theta}_1\cdot \dot{\theta}_2$$

Considering assumptions (2) and (3), the potential energy of the system is null. As a consequence we can write

$$Q_1 = \frac{d}{dt}\left(\frac{\partial K}{\partial \dot{\theta}_1}\right) - \frac{\partial K}{\partial \theta_1}$$
$$Q_2 = \frac{d}{dt}\left(\frac{\partial K}{\partial \dot{\theta}_2}\right) - \frac{\partial K}{\partial \theta_2}$$

By definition, $Q_1 = \tau_1$. Further calculation of Q_1 yields

$$\frac{\partial K}{\partial \dot{\theta}_1} = \left(\mathrm{I} + \frac{3}{4}\cdot \mathrm{m}\cdot \mathrm{L}^2\right) + \mathrm{m}\cdot \mathrm{L}^2\cdot \cos(\theta_2 - \theta_1)\cdot \dot{\theta}_2$$
$$\frac{d}{dt}\left(\frac{\partial K}{\partial \dot{\theta}_1}\right) = \mathrm{m}\cdot \mathrm{L}^2\cdot \cos(\theta_2 - \theta_1)\cdot \ddot{\theta}_2 - \mathrm{m}\cdot \mathrm{L}^2\cdot \sin(\theta_2 - \theta_1)\cdot (\dot{\theta}_2 - \dot{\theta}_1)\cdot \dot{\theta}_2$$
$$\frac{\partial K}{\partial \theta_1} = \left(\mathrm{I} + \frac{3}{4}\cdot \mathrm{m}\cdot \mathrm{L}^2\right)\cdot \ddot{\theta}_1 + \mathrm{m}\cdot \mathrm{L}^2\cdot \sin(\theta_2 - \theta_1)\cdot \dot{\theta}_1\cdot \dot{\theta}_2$$

$$Q_1 = \tau_1 = \left(\mathrm{I} + \frac{3}{4}\cdot \mathrm{m}\cdot \mathrm{L}^2\right)\cdot \ddot{\theta}_1 + \mathrm{m}\cdot \mathrm{L}^2\cdot \cos(\theta_2 - \theta_1)\cdot \ddot{\theta}_2 - \mathrm{m}\cdot \mathrm{L}^2\cdot \sin(\theta_2 - \theta_1)\cdot \dot{\theta}_2^{\,2}$$

Symmetrically

$$Q_2 = \tau_2 = \left(\mathrm{I} + \frac{3}{4}\cdot \mathrm{m}\cdot \mathrm{L}^2\right)\cdot \ddot{\theta}_2 + \mathrm{m}\cdot \mathrm{L}^2\cdot \cos(\theta_2 - \theta_1)\cdot \ddot{\theta}_1 - \mathrm{m}\cdot \mathrm{L}^2\cdot \sin(\theta_2 - \theta_1)\cdot \dot{\theta}_1^{\,2}$$

The dynamics of the arm is finally given by

$$\begin{pmatrix}\tau_1\\ \tau_2\end{pmatrix} = \begin{pmatrix}\mathrm{A} & \mathrm{B}\cdot \cos(\theta_2 - \theta_1)\\ \mathrm{B}\cdot \cos(\theta_2 - \theta_1) & \mathrm{A}\end{pmatrix}\cdot \begin{pmatrix}\ddot{\theta}_1\\ \ddot{\theta}_2\end{pmatrix} + \begin{pmatrix}0 & -\mathrm{B}\cdot \sin(\theta_2 - \theta_1)\cdot \dot{\theta}_2\\ -\mathrm{B}\cdot \sin(\theta_2 - \theta_1)\cdot \dot{\theta}_1 & 0\end{pmatrix}\cdot \begin{pmatrix}\dot{\theta}_1\\ \dot{\theta}_2\end{pmatrix}$$

where $A = \left(I + \frac{3}{4} \cdot m \cdot L^2 \right)$ and $B = m \cdot L^2$.

Inertia

Under assumption (4), the inertia I can be calculated considering the links as rectangular plates (what is not quite exact as the links are roundish at their ends) and without taking into account the inertia of the rotational joints.

$$I = \frac{m}{12} \cdot (L^2 + l^2)$$

where l is the width of the link and L its length.

Application to the device

Knowing the arm was made of aluminium, and knowing the dimensions of the arm, the mass m and the inertia I of each link could be evaluated, in order to have an idea of the values of A and B. Using $m = \mu_{Al} \cdot \text{Volume}$, where $\mu_{Al} = 2.7\,\text{g.cm}^{-2}$ represents the density of aluminium, we found m = 22 g, and I = 0.5 kg.m^2. We could then deduce an approximate value of A and B:

$$A = 8 \cdot 10^{-4}\,\text{kg.m}^2$$

$$B = 4 \cdot 10^{-4}\,\text{kg.m}^2$$

During experiments, the parameters were calculated as followed:

- Parameter A: The maximum passive torque was applied to one link, preventing it from any motion. The dynamics will then be reduced to

$$\begin{pmatrix} \tau_1 \\ \tau_2 \end{pmatrix} = \begin{pmatrix} A \cdot \ddot{\theta}_1 \\ B \cdot \cos(\theta_2 - \theta_1) \cdot \ddot{\theta}_1 - B \cdot \sin(\theta_2 - \theta_1) \cdot \dot{\theta}_1^{\,2} \end{pmatrix}$$

Fixing τ_1 and measuring the acceleration, A can then easily be deduced: $A = 1 \cdot 10^{-3}\,\mathrm{kg.m^2}$.

Using a symmetric procedure showed the arm was symmetric regarding A.

- Parameter B: The arm was set nearly to full extension, making $\theta_1 - \theta_2 = 0$.

The dynamics will then be reduced to

$$\begin{pmatrix} \tau_1 \\ \tau_2 \end{pmatrix} = \begin{pmatrix} A & B \\ B & A \end{pmatrix} \cdot \begin{pmatrix} \ddot{\theta}_1 \\ \ddot{\theta}_2 \end{pmatrix}$$

Fixing τ_1 and τ_2, and measuring the acceleration, B can be deduced: $B = 6 \cdot 10^{-4}\,\mathrm{kg.m^2}$, and symmetry was proven.

Jacobian

To derive the Jacobian *J*, we should first derive the position of the tip, and then deduce the velocity:

$$\begin{pmatrix} x \\ y \end{pmatrix} = \begin{pmatrix} L \cdot \cos(\theta_1) + L \cdot \cos(\theta_2) \\ L \cdot \sin(\theta_1) + L \cdot \sin(\theta_2) \end{pmatrix}$$

$$\begin{pmatrix} \dot{x} \\ \dot{y} \end{pmatrix} = \begin{pmatrix} -\dot{\theta}_1 \cdot L \cdot \sin(\theta_1) - \dot{\theta}_2 \cdot L \cdot \sin(\theta_2) \\ \dot{\theta}_1 \cdot L \cdot \cos(\theta_1) + \dot{\theta}_2 \cdot L \cdot \cos(\theta_2) \end{pmatrix}$$

Lastly, we get the Jacobian

$$J = L \cdot \begin{pmatrix} -\sin(\theta_1) & -\sin(\theta_2) \\ \cos(\theta_1) & \cos(\theta_2) \end{pmatrix}$$

Apparent mass

The apparent mass matrix is given by $M = J^T \cdot I^{-1} \cdot J$, where *M* is the apparent mass matrix, *J* the Jacobian, and I the inertia matrix. The apparent mass will therefore depend

on the configuration of the arm, and on the direction. We will estimate the apparent mass in nominal position, what results in $\theta_1 - \theta_2 = \frac{\pi}{2}$ and $\theta_1 = \frac{\pi}{4}$ Therefore we have

$$M = \left(\frac{L\sqrt{2}}{2}\right)^2 \cdot \begin{pmatrix} -1 & 1 \\ 1 & 1 \end{pmatrix}^T \cdot \begin{pmatrix} A & B \\ B & A \end{pmatrix}^{-1} \cdot \begin{pmatrix} -1 & 1 \\ 1 & 1 \end{pmatrix}$$

$$= \frac{L^2}{2} \cdot \begin{pmatrix} -1 & 1 \\ 1 & 1 \end{pmatrix} \cdot \frac{1}{A^2 - B^2} \cdot \begin{pmatrix} A & -B \\ -B & A \end{pmatrix} \cdot \begin{pmatrix} -1 & 1 \\ 1 & 1 \end{pmatrix}$$

$$= \frac{L^2}{2 \cdot (A^2 - B^2)} \cdot \begin{pmatrix} -1 & 1 \\ 1 & 1 \end{pmatrix} \cdot \begin{pmatrix} B - A & A + B \\ A - B & A + B \end{pmatrix}$$

$$= \frac{L^2}{2 \cdot (A^2 - B^2)} \cdot \begin{pmatrix} 2 \cdot (A - B) & 0 \\ 0 & 2 \cdot (A + B) \end{pmatrix}$$

$$M = \begin{pmatrix} \frac{L^2}{A + B} & 0 \\ 0 & \frac{L^2}{A - B} \end{pmatrix}$$

We can now replace the parameters by their value. We deduce 15 g for the apparent mass along x and 45 g along y.

Force profile

The force that the interface can simulate depends on the configuration of the arm. An example of the variation of the force will be given here in a particular case.

We will measure the force in the following configuration: $\theta_1 = -\theta_2$. The torques will be set such that $\tau_1 = -\tau_2 = \tau$ The formula transforming the forces at the tip in the torques

applied is given by $\tau = J^T \cdot F$ which yields $F = \left(J^T\right)^{-1} \cdot \tau$ if $\left(J^T\right)^{-1}$ is invertible. Explicitly written, it yields

$$\begin{pmatrix} F_x \\ F_y \end{pmatrix} = \frac{1}{\mathrm{L}\sin(\theta_2 - \theta_1)} \cdot \begin{pmatrix} \cos(\theta_2) & -\cos(\theta_1) \\ \sin(\theta_2) & -\sin(\theta_1) \end{pmatrix} \cdot \begin{pmatrix} \tau_1 \\ \tau_2 \end{pmatrix}.$$

In our particular configuration, we have

$$\begin{pmatrix} F_x \\ F_y \end{pmatrix} = \frac{1}{\mathrm{L}\sin(2 \cdot \theta_2)} \cdot \begin{pmatrix} \cos(\theta_2) & -\cos(\theta_2) \\ \sin(\theta_2) & \sin(\theta_2) \end{pmatrix} \cdot \begin{pmatrix} \tau \\ -\tau \end{pmatrix}$$

$$\begin{pmatrix} F_x \\ F_y \end{pmatrix} = \frac{1}{\mathrm{L}\sin(2 \cdot \theta_2)} \cdot \begin{pmatrix} 2 \cdot \cos(\theta_2) \cdot \tau \\ 0 \end{pmatrix}$$

The resulting force can be measured along the x axis.

The distance *d* of the tip from the actuating base of the arm is given by:

$$d = \sqrt{(\mathrm{L} \cdot (\cos(\theta_1) + \cos(\theta_2))^2 + (\mathrm{L} \cdot (\sin(\theta_1) + \sin(\theta_2))^2} \ .$$

After reduction, it gives:

$$d = 2 \cdot \mathrm{L} \cdot \cos(\theta_2) \quad (4)$$

Now, we will modify the expression of F_x:

$$\begin{aligned} F_x &= \frac{2 \cdot \cos(\theta_2)}{\mathrm{L} \cdot \sin(2 \cdot \theta_2)} \cdot \tau \\ &= \frac{2 \cdot \cos(\theta_2)}{2 \cdot \mathrm{L} \cdot \sin(\theta_2) \cdot \cos(\theta_2)} \cdot \tau \\ &= \frac{\tau}{\mathrm{L} \cdot \sin(\theta_2)} \\ &= \frac{\tau}{\mathrm{L} \cdot \sqrt{1 - \cos^2(\theta_2)}} \\ F_x &= \frac{\tau}{\mathrm{L}} \cdot \frac{1}{\sqrt{1 - \frac{d^2}{4 \cdot L^2}}} \end{aligned}$$

We can see how the force changes when the distance changes. The curve is plotted in Figure A.2. We can see that the experimental result is quite close to the prediction. There are therefore no significant losses in the transmission of forces due to the structure of the arm or to the rotational joints between the links.

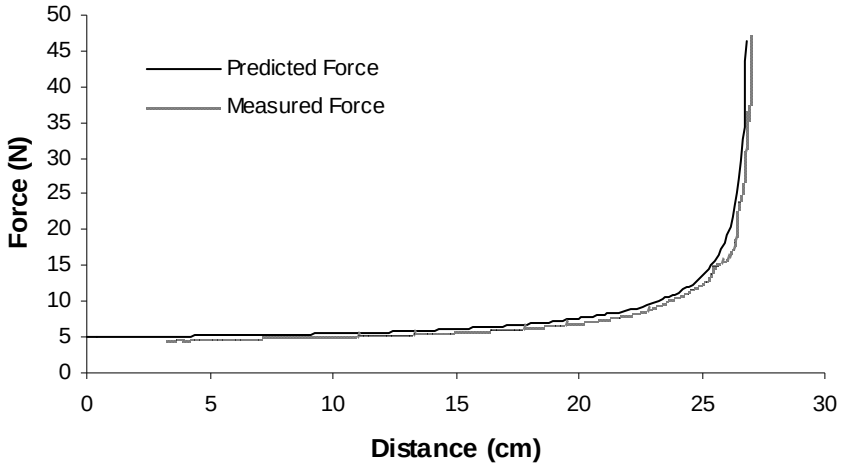

Figure A.2: Force at the tip vs distance from center of rotation

Force-field simulation

The implementation of force-fields requires us to use the relation transforming the motor torques in the force at the tip of the arm. This relation is given by

$$\begin{pmatrix} \tau_1 \\ \tau_2 \end{pmatrix} = \mathrm{L} \cdot \begin{pmatrix} -\sin(\theta_1) & \cos(\theta_1) \\ -\sin(\theta_2) & \cos(\theta_2) \end{pmatrix} \cdot \begin{pmatrix} F_x \\ F_y \end{pmatrix}.$$

So for a given force F, the USM torques τ_1 and τ_2 can be computed using the equation above.